

ผลกระทบจากความขรุขระของผิวฟิล์มบาง $\text{CuIn}_{1-x}\text{Ga}_x\text{Se}_2$ ในการพอกพูนฟิล์มบางของ CdS ใน
อ่างเคมี

นายแทนชนก มุ้ยแพง



จุฬาลงกรณ์มหาวิทยาลัย
CHULALONGKORN UNIVERSITY

บทคัดย่อและแฟ้มข้อมูลฉบับเต็มของวิทยานิพนธ์ตั้งแต่ปีการศึกษา 2554 ที่ให้บริการในคลังปัญญาจุฬาฯ (CUIR)

เป็นแฟ้มข้อมูลของนิสิตเจ้าของวิทยานิพนธ์ ที่ส่งผ่านทางบัณฑิตวิทยาลัย

วิทยานิพนธ์นี้เป็นส่วนหนึ่งของการศึกษาตามหลักสูตรปริญญาวิทยาศาสตรมหาบัณฑิต

The abstract and full text of theses from the academic year 2011 in Chulalongkorn University Intellectual Repository (CUIR) are the thesis authors' files submitted through the University Graduate School.

สาขาวิชาฟิสิกส์ ภาควิชาฟิสิกส์

คณะวิทยาศาสตร์ จุฬาลงกรณ์มหาวิทยาลัย

ปีการศึกษา 2559

ลิขสิทธิ์ของจุฬาลงกรณ์มหาวิทยาลัย

Effects of $\text{CuIn}_{1-x}\text{Ga}_x\text{Se}_2$ Thin Film Surface Roughness in Chemical Bath Deposition
of CdS Thin Films

Mr. Tanchanok Muifeang



A Thesis Submitted in Partial Fulfillment of the Requirements
for the Degree of Master of Science Program in Physics

Department of Physics

Faculty of Science

Chulalongkorn University

Academic Year 2016

Copyright of Chulalongkorn University

Thesis Title Effects of $\text{CuIn}_{1-x}\text{Ga}_x\text{Se}_2$ Thin Film Surface
Roughness in Chemical Bath Deposition of CdS
Thin Films

By Mr. Tanchanok Muifeang

Field of Study Physics

Thesis Advisor Assistant Professor Dr. Sojiphong Chatraphorn,
Ph.D.

Accepted by the Faculty of Science, Chulalongkorn University in Partial
Fulfillment of the Requirements for the Master's Degree

..... Dean of the Faculty of Science
(Associate Professor Dr. Polkit Sangvanich, Ph.D.)

THESIS COMMITTEE

..... Chairman
(Assistant Professor Dr. Rattachat Mongkolnavin, Ph.D.)

..... Thesis Advisor
(Assistant Professor Dr. Sojiphong Chatraphorn, Ph.D.)

..... Examiner
(Assistant Professor Dr. Sakuntam Sanorpim, Ph.D.)

..... External Examiner
(Dr. Rachsak Sakdanuphab)

แทนชนัก มุ่ยแฝง : ผลกระทบจากความขรุขระของผิวฟิล์มบาง $\text{CuIn}_{1-x}\text{Ga}_x\text{Se}_2$ ในการพอกพูนฟิล์มบางของ CdS ในอ่างเคมี (Effects of $\text{CuIn}_{1-x}\text{Ga}_x\text{Se}_2$ Thin Film Surface Roughness in Chemical Bath Deposition of CdS Thin Films) อ.ที่ปรึกษา วิทยานิพนธ์หลัก: ผศ. ดร. โสจิงค์ ฉัตรภรณ์, 85 หน้า.

เซลล์สุริยะชนิดฟิล์มบาง $\text{CuIn}_{1-x}\text{Ga}_x\text{Se}_2$ (CIGS) บนแผ่นรองรับกระจก (SLG) ประกอบด้วยชั้นฟิล์มบางชนิด 6 ชั้น; SLG/Mo/CIGS/CdS/i-ZnO/ZnO(Al)/Al-grid ในงานวิจัยนี้ได้ทำการปรับปรุงรอยต่อระหว่างฟิล์ม CIGS และฟิล์ม CdS โดยการปรับเปลี่ยนผิวฟิล์ม CIGS ด้วยสารเคมีชนิดต่างๆ ได้แก่ เอควารีเจีย, โพลแทสเซียมไฮดรอกไซด์ และ แอลกอฮอล์ลิทโพแทสเซียมไฮดรอกไซด์ ผิวฟิล์ม CIGS ที่ถูกปรับเปลี่ยนแล้ว จะถูกตรวจสอบโดยกล้องจุลทรรศน์อิเล็กตรอนแบบส่องกราด และกล้องจุลทรรศน์แรงอะตอม ในแง่ของสัญญาณวิทยา และค่า rms roughness ตามลำดับ ซึ่งพบว่า เอควารีเจียสามารถปรับเปลี่ยนผิว CIGS ได้อย่างมีประสิทธิภาพ ขณะที่สารเคมีชนิดอื่นไม่สามารถสังเกตเห็นการเปลี่ยนแปลงที่ผิว CIGS ได้อย่างชัดเจน โดยการวิเคราะห์กราฟความสัมพันธ์ระหว่างความหนาแน่นของกระแสสูงที่สุดกับความต่างศักย์สูงที่สุด และกราฟประสิทธิภาพเชิงควอนตัม แสดงให้เห็นว่าการกัดผิวด้วยโพแทสเซียมไฮดรอกไซด์ และแอลกอฮอล์ลิทโพแทสเซียมไฮดรอกไซด์แสดงสมรรถนะของเซลล์สุริยะที่ต่ำกว่าเงื่อนไขการกัดด้วยเอควารีเจีย ซึ่งเปรียบเทียบกับเงื่อนไขที่ยังไม่ได้กัด ดังนั้นความเข้มข้น และช่วงเวลาการกัด ด้วยเอควารีเจียจึงถูกนำมาศึกษา โดยจากการทดลองพบว่า การใช้สารละลายเอควารีเจียที่มีอัตราส่วนระหว่างเอควารีเจียต่อน้ำบริสุทธิ์ปราศจากไอออนเป็น 1:1 ด้วยเวลาการกัดสั้นๆ สามารถสร้างความขรุขระของผิวฟิล์ม CIGS ที่เหมาะสมสำหรับรอยต่อฟิล์ม CIGS และ CdS ได้ กระบวนการนี้ได้ถูกนำมาใช้ในกระบวนการผลิตเซลล์สุริยะชนิด CIGS ในแง่ของการพัฒนาสมรรถนะของเซลล์สุริยะ

ภาควิชา ฟิสิกส์

สาขาวิชา ฟิสิกส์

ปีการศึกษา 2559

ลายมือชื่อนิติศ

ลายมือชื่อ อ.ที่ปรึกษาหลัก

5671972623 : MAJOR PHYSICS

KEYWORDS: CIGS SURFACE ROUGHNESS / CHEMICAL ETCHING / CIGS SOLAR CELL

TANCHANOK MUIFEANG: Effects of $\text{CuIn}_{1-x}\text{Ga}_x\text{Se}_2$ Thin Film Surface Roughness in Chemical Bath Deposition of CdS Thin Films. ADVISOR: ASST. PROF. DR. SOJIPHONG CHATRAPHORN, Ph.D., 85 pp.

Typical $\text{CuIn}_{1-x}\text{Ga}_x\text{Se}_2$ (CIGS) thin film solar cells on soda-lime glass (SLG) substrate consist of six different thin film layers; SLG/Mo/CIGS/CdS/i-ZnO/ZnO(Al)/Al-grids. In this work, the interface of CIGS/CdS film was modified by altering CIGS surface with various chemical solutions such as aqua regia, potassium hydroxide and alcoholic potassium hydroxide. The modified CIGS surface was investigated by FESEM and AFM in terms of morphology and RMS roughness, respectively. It was found that aqua regia could effectively alter the CIGS surface while the others could not visually change the surface. The J-V and external quantum efficiency (EQE) measurements showed that potassium hydroxide and alcoholic potassium hydroxide etchings resulted in lower solar cell performance than aqua regia etching when compared with the non-etched condition. The concentration and etching time using aqua regia were investigated. As a result, using 1:1 of aqua regia : deionized water at a few seconds of etching time could create an optimal CIGS surface roughness for the CIGS/CdS interface. This method was employed in the fabrication of the CIGS solar cells in order to improve its performance.

Department: Physics

Student's Signature

Field of Study: Physics

Advisor's Signature

Academic Year: 2016

ACKNOWLEDGEMENTS

First of all, I would like to express my deepest gratitude to my thesis advisor, Assistant Professor Dr. Sojiphong Chatraphorn who gave me a chance to be a part of Semiconductor Physics Research Laboratory (SPRL) members. He taught and instructed many things to do the experiments, that he is always a good model to follow. I would like to especially thank for his generosity on AFM measurements. Without his advices, this thesis cannot be succeeded. Moreover, Assistant Professor Dr. Kajornyod Yoodee, he also recommends me to explore the related books and journals.

Beside my advisor, I would like to thank my thesis committee: Assistant Professor Dr. Rattachat Mongkolnavin, Assistant Professor Dr. Sakuntum Sanorpim, and Assistant Professor Dr. Rachsak Sakdanuphab, for their beneficial suggestions and comments to fulfill this thesis.

I would like to thank my colleagues at SPRL: Miss Busarin Noikaew for her patience and dedication to teach me about fabricating steps of CIGS solar cells, especially the co-evaporation process. Miss Boonyaluk Namnuan for her supports. She persuaded and pushed on me into SPRL members. Also, Miss Kwanruthai Butsriruk for her good ideas and advices to do the experiments. Moreover, Mr. Supathat Sukaiem for his kindness to measure the spectral response of the solar cells. I would also like to thank Mr. Pornsak Panchawirat from the Thailand Center of Excellence in Physics (ThEP center) for theoretical knowledges and helping with FESEM images, which he took more than a hundred of images in this study.

Especially, I would like to acknowledge the financial supports from the ThEP center, the Special Task Force for Activating Research (STAR), Ratchadaphiseksompot Endowment Fund, Chulalongkorn University through the Energy Materials Physics Research Group. Finally, morale encouragement from my family for studying in master degree is a precious thing in my life that I cannot forget to thank and appreciate.

CONTENTS

	Page
THAI ABSTRACT	iv
ENGLISH ABSTRACT.....	v
ACKNOWLEDGEMENTS.....	vi
CONTENTS.....	vii
LIST OF TABLES	1
LIST OF FIGURES	2
LIST OF SYMBOLS AND ABBREVIATIONS	5
CHAPTER I INTRODUCTION.....	8
1.1 Overview.....	8
1.2 Objectives	14
1.3 Thesis outline.....	14
CHAPTER II THEORETICAL BACKGROUNDS.....	15
2.1 Principle of solar cell	15
2.1.1 Basic Theory of Semiconductor Materials	15
2.1.2 Principles of Solar Cells	20
2.2 $\text{CuIn}_{1-x}\text{Ga}_x\text{Se}_2$	23
2.2.1 Fundamental properties	23
2.2.2 $\text{CuIn}_{1-x}\text{Ga}_x\text{Se}_2$ based-thin film solar cells	26
2.3 The Multi-Source Co-Evaporation	28
2.3.1 Multi-Source Co-Evaporation System	28
2.3.2 Three-Stage Co-Evaporation	30
2.3.3 Calculation of the CIGS deposition rate.....	31
2.4 Chemical Etching Processes	34
2.4.1 Wet-etching method	34
CHAPTER III EXPERIMENTAL PROCEDURES.....	37
3.1 CIGS Solar Cell Fabrication	37
3.1.1 Substrate preparation.....	37
3.1.2 Mo back contact	38

	Page
3.1.3 CIGS absorber	38
3.1.4 CdS buffer	40
3.1.5 ZnO window	42
3.1.6 Al-grids.....	43
3.2 Wet-Etching Method	44
3.2.1 Aqua regia	44
3.2.2 Potassium Hydroxide	45
3.2.3 Alcoholic Potassium Hydroxide.....	47
3.3 Characterization Techniques	48
3.3.1 Scanning Electron Microscopy (SEM).....	48
3.3.2 Atomic Force Microscopy (AFM)	50
3.3.3 Current-Voltage (I-V) Measurement.....	51
3.3.4 External Quantum Efficiency (EQE) Measurement.....	52
CHAPTER IV RESULTS AND DISCUSSION.....	54
4.1 Surface morphology and RMS roughness	54
4.2 J-V curves	68
4.3 Spectral responses.....	76
CHAPTER V SUMMARY	79
REFERENCES	81
VITA.....	85

LIST OF TABLES

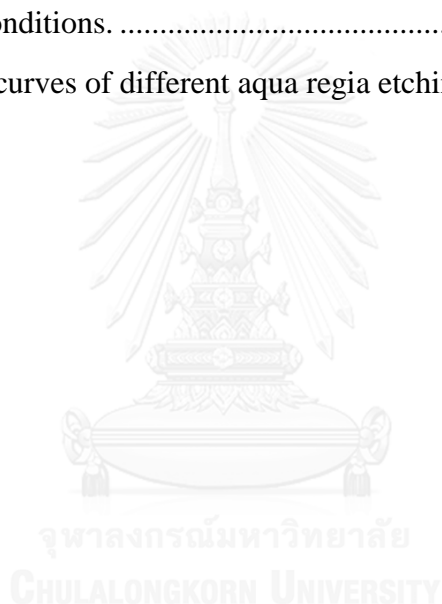
	Page
Table 1 Density and molecular mass of the material used in CIGS fabrication process	34
Table 2 The applications of each chemical types.....	35
Table 3 The aqua regia etching conditions by varying etching times.	45
Table 4 The potassium hydroxide conditions by varying etching times.....	47
Table 5 The alcoholic potassium hydroxide conditions by varying etching times. ...	48
Table 6 Current loss, $\Delta 1.12$ eV due to the optical and collection losses illustrated in Figure 28 for a typical Cu(In,Ga)Se ₂ /CdS solar cell.....	53
Table 7 The FESEM and AFM results of potassium hydroxide (KOH) etching conditions.	55
Table 8 The FESEM and AFM results of alcoholic potassium hydroxide (KOH+EtOH) etching conditions.....	57
Table 9 The FESEM and AFM results of aqua regia etching conditions.	59
Table 10 The comparison of surface morphology and rms roughness results of aqua regia, KOH, and KOH+EtOH etching conditions.....	61
Table 11 The different aqua regia etching conditions by varying concentrations and etching times.....	62
Table 12 The FESEM and AFM results of different aqua regia conditions by varying concentrations and etching times.	63
Table 13 The FESEM images of different aqua regia etching conditions with 30,000 \times and 100,000 \times magnification.	66
Table 14 The rms roughness values and solar cell parameters of potassium hydroxide and alcoholic potassium hydroxide etching conditions.	70
Table 15 The rms roughness values and solar cell parameters of different aqua regia etching conditions.....	72

LIST OF FIGURES

		Page
Figure 1	The worldwide growth of photovoltaic since 1992	8
Figure 2	The lattice spacing of the (112) planes of $\text{CuIn}_{1-x}\text{Ga}_x\text{Se}_2$ and the (111) cubic or the (002) hexagonal planes of $\text{Cd}_{1-x}\text{Zn}_x\text{S}$	10
Figure 3	The efficiency of $\text{Cu}(\text{In,Ga})\text{Se}_2$ solar cells with a selection of Cd-free junction formation methods together with corresponding values of $\text{Cu}(\text{In,Ga})\text{Se}_2$ cells with CBD of CdS	11
Figure 4	Expected models for chemical etching of CIGS surface.	14
Figure 5	Density of states functions, Fermi-Dirac probability function, and areas representing electron and hole concentration for the case when E_F is near the mid-gap energy	15
Figure 6	(a) Two-dimensional representation of the silicon lattice doped with a phosphorus atom; (b) The energy-band diagram showing the effect of a donor state being ionized; (c) Density of states functions, Fermi-Dirac probability function, and areas representing electron and hole concentration for the case when E_F is above the intrinsic Fermi energy ..	19
Figure 7	(a) Two-dimensional representation of the silicon lattice showing the ionization of the boron atom resulting in a hole; (b) The energy-band diagram showing the effect of a acceptor state being ionized; (c) Density of states functions, Fermi-Dirac probability function, and areas representing electron and hole concentration for the case when E_F is below the intrinsic Fermi energy	20
Figure 8	A p-n junction solar cell with resistive load.	21
Figure 9	I-V characteristics of a p-n junction solar cell.	21
Figure 10	The unit cell of the chalcopyrite lattice structure	23
Figure 11	Ternary phase diagram of the Cu-In-Se system. Thin-film composition is usually near the pseudo-binary $\text{Cu}_2\text{Se}-\text{In}_2\text{Se}_3$ tie line	24
Figure 12	Pseudo-binary $\text{In}_2\text{Se}_3-\text{Cu}_2\text{Se}$ equilibrium phase diagram for compositions around the CuInSe_2 chalcopyrite phase (α), The δ phase is the high-temperature sphalerite phase, and the β is as ordered defect phase (ODC). Cu_2Se exists as a room-temperature (RT) or high-temperature (HT) phase	24

Figure 13	Absorption coefficient versus photon energy of various semiconducting materials.....	25
Figure 14	The theoretical efficiencies of various solar cell materials	26
Figure 15	One-dimensional energy band diagram of the ZnO/CdS/CIGS heterojunction showing p-n junction and surface defect layer (SLD) together with inter recombination center at the CdS/CIGS interface	27
Figure 16	The multi-source co-evaporation system with the in situ monitoring.	29
Figure 17	The example growth profile in a display monitor from co-evaporation system, e.g. three-stage process.	29
Figure 18	Metal fluxes of three-stage process used to fabricate the CIGS film, including the substrate temperature profile used during the film growth.	30
Figure 19	The CIGS thin film compositions profile in three-stage process.	31
Figure 20	The graphs of evaporation rate versus elemental temperature of Cu (a), In (b) and Ga (c) sources to obtain a and b parameters by least-square fit which detected by QCM.	32
Figure 21	The FESEM image of as-grown Mo surface.	38
Figure 22	Temperature profile for the three-stage co-evaporation of CIGS thin film.	39
Figure 23	The FESEM images of as-grown CIGS surface (left) and cross-sectional view (right).	40
Figure 24	The completed CIGS solar cell device.	43
Figure 25	The SEM image of the surface of crystalline-silicon (c-Si) wafer after etching by dipping in a solution of H ₂ O/KOH/IPA (Isopropanal).....	48
Figure 26	The typically schematic diagram of SEM column	49
Figure 27	The principle of atomic force microscopy (AFM)	50
Figure 28	Quantum efficiency (solid lines) at 0 V and -1 V and optical losses for a Cu(InGa)Se ₂ /CdS solar cell in which the Cu(In,Ga)Se ₂ has E _g = 2.12 eV	53
Figure 29	The J-V curves of potassium hydroxide etching conditions.....	68
Figure 30	The J-V curves of alcoholic potassium hydroxide etching conditions.....	69
Figure 31	The J-V curves of aqua regia etching conditions.	69
Figure 32	The J-V curves of different aqua regia etching conditions.....	71

- Figure 33** The trends of short-circuit current density (J_{sc}) vs. rms roughness of different aqua regia etching conditions.74
- Figure 34** The trends of open-circuit voltage (V_{oc}) vs. rms roughness of different aqua regia etching conditions.74
- Figure 35** The trends of fill factor (FF) vs. rms roughness of different aqua regia etching conditions.75
- Figure 36** The trends of efficiency (η) vs. rms roughness of different aqua regia etching conditions.75
- Figure 37** The EQE curves of potassium hydroxide (KOH) etching conditions.76
- Figure 38** The EQE curves of alcoholic potassium hydroxide (KOH+EtOH) etching conditions.77
- Figure 39** The EQE curves of different aqua regia etching conditions.77



LIST OF SYMBOLS AND ABBREVIATIONS

α	Chalcopyrite phase
β	Ordered defect phase
δ	High-temperature sphalerite phase
η	Solar cell efficiency
a-Si	Amorphous Silicon
AFM	Atomic force microscopy
A.M.1.5	Air-mass 1.5
CBD	Chemical bath deposition
CdS	Cadmium Sulphide
CdTe	Cadmium Telleride
CIGS	Copper Indium Gallium Diselenide
c-Si	Crystalline Silicon
Cu ₂ Se	Dicopper Selenide
E_c	Conduction band edge
E_F	Fermi energy
E_{Fi}	Intrinsic Fermi energy
E_g	Band gap energy
EQE	External quantum efficiency
E_v	Valence band edge
$f_E(E)$	Fermi-Dirac probability function
FF	Fill factor
$g_c(E)$	Density of quantum state in conduction band

$g_v(E)$	Density of quantum state in valence band
HT	High temperature
H ₂ Se	Dihydrogen Selenide
i-CdS	Intrinsic Cadmium Sulphide
I _F	Forward-bias current
I _L	Photocurrent
I _m	Maximum current
InP	Indium Phosphide
IQE	Internal quantum efficiency
I _s	Device saturation current
I _{sc}	Short-circuit current
i-ZnO	Intrinsic Zinc Oxide
J _{sc}	Short-circuit current density
KOH	Potassium Hydroxide
KOH+EtOH	Alcoholic Potassium Hydroxide
Mo	Molybdenum
n ₀	Thermal-equilibrium concentration of electron
N _c	Effective density of state function in conduction band
n _i	Intrinsic carrier concentration
NREL	National Renewable Energy Laboratory
N _v	Effective density of state function in valence band
OP	Output power
ODC	Ordered defect compound
p ₀	Thermal-equilibrium concentration of hole

PBN	Pyrolytic Boron Nitride
PID	Propoartional-Integral-Derivation
P_{in}	Incident optical power
P_m	Maximum output power
PV	Photovoltaic
QCM	Quartz crystal microbalance
R_s	Serie resistance
R_{sh}	Shunt resistance
RT	Room temperature
SCR	Space charge region
SDL	Surface defect layer
SLG	Soda-lime glass
SQ	Shockley-Queisser
T1	Substrate temperature at 1 st stage of three-stage growth profile
T2	Substrate temperature at 2 nd and 3 rd stages of three-stage growth profile
T_{pyro}	Pyrometer temperature
T_{sub}	Substrate temperature
WCE	Wet-chemical etching
x	$[Ga]/([In]+[Ga])$
y	$[Cu]/([In]+[Ga])$
ZnO(Al)	Aluminum doped zinc oxide

CHAPTER I

INTRODUCTION

1.1 Overview

The Sun is the most important source of energy for life on Earth. It gives the energy to our world in terms of sunlight, called “solar energy”. Solar energy always influences the natural phenomena that happen on the Earth. It incidences onto the Earth’s surface with the rate of 120×10^{15} Watt, so in one day it can satisfy our needs in order to consume the energy more than 20 years [1]. Moreover, the solar energy is clean, friendly to the environments, and without releasing pollutions, it is grouped in the kind of renewable energy, e.g. sunlight, wind, rain, tidal and geothermal heat. These energies will eventually replace the conventional energy source which is mostly obtained from fossil fuel. In 2012, the renewable energy was consumed about 19% of our global energy consumption, especially the solar energy that has high level of consumption among the other renewable energies in every years [2]. Recently, a statistic shows that the worldwide growth of photovoltaics tend to continuously increase every year as shown in Fig.1. Consequently, the solar energy is one of choices for energy consumption.

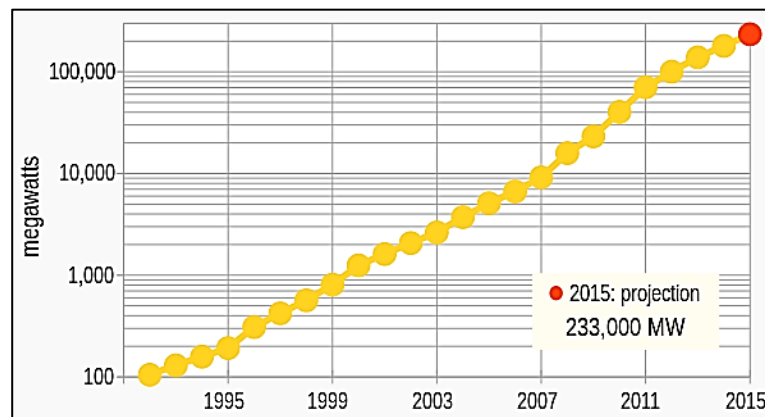


Figure 1 The worldwide growth of photovoltaic since 1992 [2].

Historically, human began to seriously apply the solar energy in steads of fossil fuel in the middle of 20th century. The device which it can alter the solar energy to the electricity, called “photovoltaic or PV”. The first solar cell (for individual PV element) was invented by D. Chapin, C. Fuller, and G. Pearson at Bell Labs in 1954, they produced a silicon solar cell with 4% efficiency [3]. Photovoltaics convert solar radiation into direct current electricity using semiconductors when illuminated by light (photon). As long as light is shining on the solar cell, it generates electrical power which measured in the unit of Watt (W) or kiloWatt (kW). When the light stops, the electricity stops. The popular semiconductors for manufacturing solar cell such as crystalline Si (c-Si), amorphous Si (a-Si), GaAs, InP, CdTe, and CIGS. For CIGS based-thin film solar cell, it uses a CIGS semiconductor as a p-type absorber layer. Interestingly, it has the unique absorption property and high energy conversion efficiency. Moreover, it has many techniques to fabricate, leading to be a promising candidate for photovoltaic application.

In the CIGS solar cell device, most of light is absorbed in the p-type CIGS layer, and the generated electrons are swept into the n-type region by the built-in field of the n-ZnO/i-CdS/p-CIGS heterojunction. The device characteristics indicate that large band bending occurs in CIGS near the CdS/CIGS interface, it converts the CIGS surface to n-type which called ordered defect compound (ODC). This band bending make effective collection of photo generated electrons possible. And the Cd_{Cu} defects heavily dope CIGS surface as n-type during chemical bath deposition (CBD) of CdS [4]. The deposition of CdS thin film becomes one of the key process in fabrication of CIGS solar cells because the CdS/CIGS junction has a large effect to the efficiencies of solar cells [5]. CdS is a metal chalcogenide semiconductors with 2.42 eV of band gap energy which it makes a large difference in the band gap between an absorber layer and a window layer. The CBD process is generally used to deposit CdS thin film, which it is a simple process that has a low cost, low temperature reaction, the potential for large-area deposition, and especially reproducibly depositing uniform thin films [6], [7], [8]. At the present, it appears

to be the best technique to deposit CdS in high efficiency CIGS thin film solar cells [8].

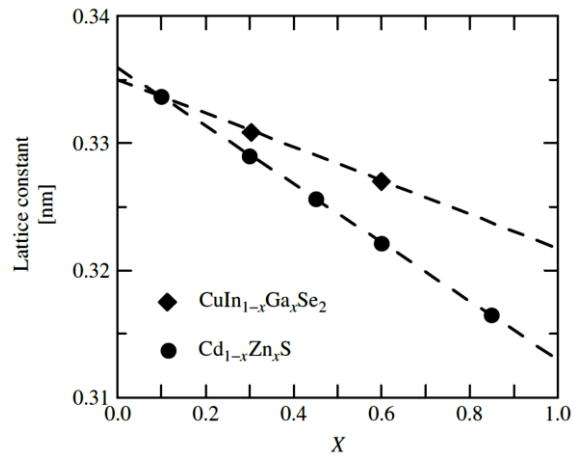


Figure 2 The lattice spacing of the (112) planes of $\text{CuIn}_{1-x}\text{Ga}_x\text{Se}_2$ and the (111) cubic or the (002) hexagonal planes of $\text{Cd}_{1-x}\text{Zn}_x\text{S}$ [9].

Both CdS buffer and ODC layers at the CIGS surface can be considered as n-type layer. The interface between CBD-CdS/CIGS layers exhibited that the (112) chalcopyrite CIGS planes parallel to the (111) cubic or hexagonal CdS planes. The lattice mismatch is very small for CIGS with a (112) spacing of 0.334 nm as compared to a spacing of 0.336 nm for (111) cubic and (002) hexagonal CdS. Indeed, the lattice mismatch increases with Ga content or $x = [\text{Ga}]/([\text{In}] + [\text{Ga}])$ [9]. In the initial stage of CBD-CdS, it showed the presence of Cd up to 10 nm into the Cu-deficient surface region of CIGS layer. At the same time, the Cu^+ is replaced with Cd^{2+} that they have very close ion radii of 0.96 Å and 0.97 Å, respectively [10]. However, the CdS/CIGS interface issues are not clear. One reason comes from the CdS layer, it is a very thin layer which difficultly characterize to reveal what happens. Likewise, the ODC has a low carrier concentration, moreover it may not exist on the CIGS film surface at all [11]. Nevertheless, the CdS buffer can efficiently help to protect ion damage during n-ZnO window layer manufacturing. Alternative buffers such as $\text{Zn}(\text{O},\text{S})$ and $\text{In}_x(\text{OH},\text{S})_y$ are required for replacing of CdS buffer layer because it is a

toxic material [12]. But, CdS still reaches better results in term of solar cell performance and especially the p-n junction formation.

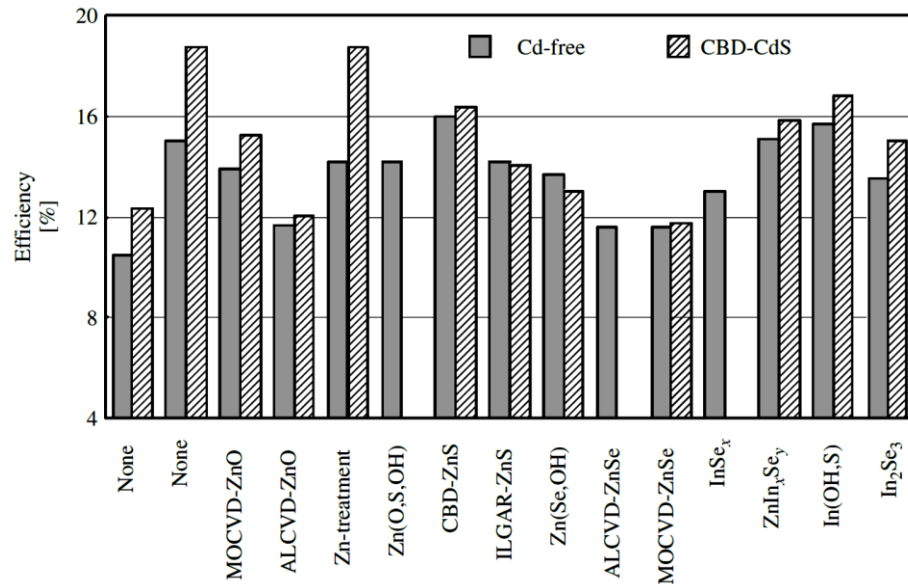


Figure 3 The efficiency of Cu(In,Ga)Se₂ solar cells with a selection of Cd-free junction formation methods together with corresponding values of Cu(In,Ga)Se₂ cells with CBD of CdS [9].

Noticeably, the role of the roughness at the interface between CIGS-absorber and CdS-buffer layers is an attractive factor. It is naturally fixed by the as-grown CIGS surface which usually depends on CIGS growth condition. The roughness of CIGS surface affects the solar cell properties such as light trapping or scattering, p-n junction formation, and especially the solar cell parameters [5], [13], [14]. Understanding the relationship between the roughness of CIGS surface and solar cell parameters may help for future improvements.

Several attempts have been tried to study the CIGS/CdS interface in order to improve the solar cell performance. One of those is the modification of CIGS surface roughness because it directly affects the CdS formation and also influences the efficiency of the solar cells [5], [10], [13]. The wet-chemical etching (WCE) is one of several methods used to alter the CIGS surface roughness. The WCE process is to etch the material surface in the liquid etchant.

This method is generally used in different kind of electronic device fabrication industries [15]. For thin film photovoltaic industries, wet-etching process is used to modify the film surface. By submerging the substrate in a solution that will chemically attack their surface. The degree of etching is particularly high, which makes the etching rapid.

In case of CIGS thin film, R.W. Birkmire *et. al.* showed an aqueous solution of bromine (Br_2) etching for the propose of obtaining specular CuInSe_2 (CIS) surfaces. By varying the concentration range from 0.02 mol/L to 0.25 mol/L. The etching rates observed by ranging from 0.1 to 5 $\mu\text{m}/\text{min}$. Their modified CuInSe_2 surfaces are desired in order to improve the electrical characteristics of tandem $\alpha\text{-Si} : \text{CuInSe}_2$ cells [16]. B. Canava *et. al.* described the bromine etching for obtaining specular CIGS surface and controlling the surface composition. Their CIGS layer partially protected by resin which is submerged in a 0.001 to 1 mol/L solution of bromine in water for a few second, at ambient temperature. Then, it is treated with a solution of 0.1 mol/L of potassium cyanide (KCN) at 70 °C. Their analysis shows a thickness reduction of CIGS layer after etching, and also a variation in the composition of the CIGS layer [14]. T. Delsol *et. al.* did the experiment that etched the CIGS surface with various commonly used wet-chemical etchants such as the mixture of hydrochloric acid and nitric acid, peroxide, ammonia, thiosulphate and dicromate. They found that there is the possibility of Se-deficient surface when etched in peroxide, Se-rich surface when etched in dichromate and similar surface to the as-grown when etched in ammonia [17]. Moreover, M. Kauk *et. al.* used hydrochloric acid, potassium cyanide, potassium hydroxide in ethanol and also ammonia to alter the CuInSe_2 monograin layer. They revealed that with long-time ammonia etching showed undesirable results to the solar cell performance, while potassium cyanide etching before CBD-CdS resulted in improved solar cell performance for both Cu-rich and In-rich types. For hydrochloric acid etching, it removes preferably In and leaves slightly Se-rich surface. And the solar cell would shows the higher current but lower open-circuit voltage when compare with the as-grown cell. In case of potassium

hydroxide in ethanol, it can help to remove the excess selenium from the CuInSe₂ monograin layer, but the solar cell gave lower open-circuit voltage and also short-circuit current at 5 seconds of etching time [18]. A. Slobodskyy *et. al.* used aqua regia solution to etch the CIGS surface which found that the etching rate is approximately 10 nm/sec of 3 minutes after preparation of the acid. Z. Jehl *et. al.* reported the thinning of the CIGS layer using Br-based etching process. The total reflectivity of the CIGS surface increases with decreasing roughness whereas current density would decrease and especially efficiencies markedly decrease from 14 % down to 11 %, even for more than 2 μm thick solar cell. They also reported that the decrease of roughness has no significant influence on crystal structure and surface composition of CIGS layer [19], [20]. Recently, Wang *et. al.* demonstrated the large-scale micro- and nano patterns of CIGS thin film solar cells by molds-assisted chemical-etching process using bromine methanol etchant that the CIGS micro-dome arrays can improve the photocurrent densities, fill factors, and efficiencies, while the CIGS micro-hole arrays give lower quality of solar cell [21]. Hence, we can initially conclude that the rod shape of CIGS surface will give a better result than the hole shape surface. However, bromine is highly toxic. In a form of solution or vapor, bromine can extremely damage human health especially by inhalation [22]. As-mentioned above, there are also many attempts tried to alter the CIGS surface roughness with the other solutions such as aqua regia, ammonia, sulfuric acid, peroxide, potassium hydroxide, etc., but the results did not achieve high performance CIGS solar cell [13], [17], [23].

For this work, attempts have been made to figure out more details about the altering of CIGS surface by using chemical etchants in various concentrations and etching times. The interface of CdS/CIGS film was modified by altering CIGS surface with various chemical solutions such as aqua regia, potassium hydroxide (KOH), and alcoholic potassium hydroxide (KOH+EtOH). The devices were completed with the depositions of CBD-CdS/i-ZnO/ZnO(Al) and followed by thermal evaporation of aluminum as the front contacts. Both i-ZnO and ZnO(Al) layers are deposited on the top of CdS

layer by radio-frequency (RF) sputtering technique. The altered CIGS surfaces were investigated for their morphologies by field-emission scanning electron microscopy (FESEM). The atomic force microscope (AFM) was used to measure the rms roughness of etched CIGS surface. In addition, current-voltage (I-V) and external quantum efficiency (EQE) measurements are employed to obtain the solar cell parameters and spectral responses, respectively.

1.2 Objectives

1. To find suitable method to alter the surface of CIGS film for chemical bath deposition (CBD) of CdS.
2. To relate the roughness of CdS and CIGS interface to the efficiencies of the solar cells.

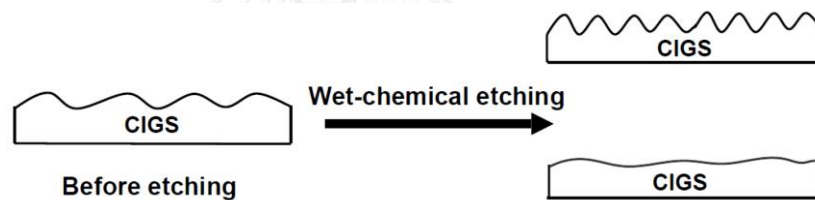


Figure 4 Expected models for chemical etching of CIGS surface.

1.3 Thesis outline

In this thesis, it is divided into five chapters. The theoretical backgrounds, including the photovoltaic effect, material properties of CIGS, the multi-sources co-evaporation and characterization techniques, and also WCE process are introduced. The experimental procedures and some information about chemical etching solutions are then described in chapter III. After that, the results that can be divided into three subtopics are discussed in chapter IV. Lastly, the final chapter is the summary of this study.

CHAPTER II

THEORETICAL BACKGROUNDS

2.1 Principle of solar cell

2.1.1 Basic Theory of Semiconductor Materials

The heart of solar cell is the p-n junction. It is made of semiconducting materials, which have a weakly bounded electron occupying band of energy called the “valence band”. When photons with energy more than a certain threshold energy called the “band gap”, are applied to valence electrons (electron in valence band), the bonds are broken and the electrons can freely move around in a new energy band called the “conduction band” where they can conduct electricity through the material. Semiconductors have two main types, called “intrinsic semiconductor” and “extrinsic semiconductor”.

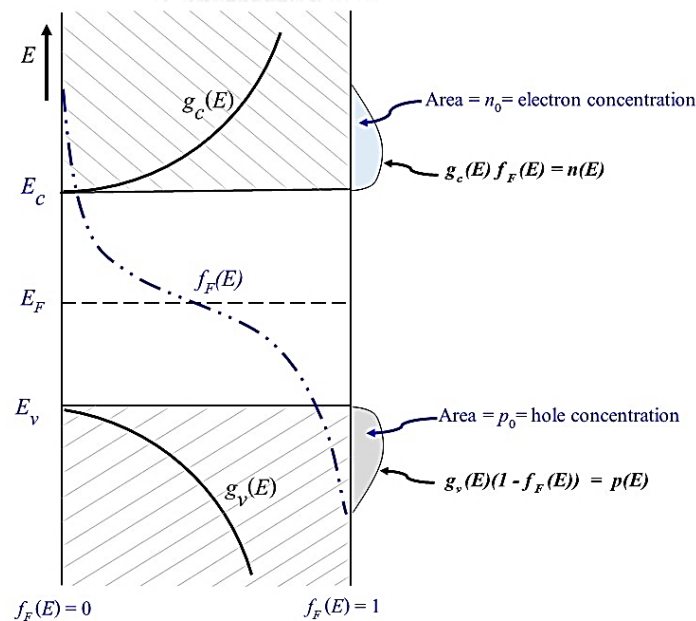


Figure 5 Density of states functions, Fermi-Dirac probability function, and areas representing electron and hole concentration for the case when E_F is near the mid-gap energy [24].

An ideal intrinsic semiconductor is a pure semiconductor with no impurity atoms and no lattice defects in the crystal (e.g. pure silicon), the number of electron carriers in the conduction band is equal to the number of hole carriers in the valence band. An important characteristic of a semiconductor is the density of charge carriers. The density of electrons and holes are related to the density of state function and the Fermi-Dirac distribution function. Fig.5 shows a plot of the density of states function in the conduction-band ($g_c(E)$), the density of states function in the valence-band ($g_v(E)$), and the Fermi-Dirac probability function for $T > 0$ K when E_F is approximately halfway between E_c and E_v . The function of $f_F(E)$ for $E > E_F$ is symmetrical to the function of $1-f_F(E)$ for $E < E_F$ about the energy $E = E_F$. It can basically calculate the number of electron carriers in the conduction band by according to Eq.(2.1).

$$n_0 = \int g_c(E) f_F(E) dE, \quad (2.1)$$

where n_0 is the thermal-equilibrium concentration of electron. The $g_c(E)$ is the density of states in the conduction band and the $f_F(E)$ is the Fermi-Dirac probability function.

The Fermi-Dirac distribution describes a distribution of particles over energy states in system consisting of many identical particles that obey the Pauli-exclusion principle. This equation gives the probability that an energy state will be occupied by an electron,

$$f_F(E) = \frac{1}{1 + \exp\left(\frac{E - E_F}{kT}\right)} \approx \exp\left[-\frac{(E - E_F)}{kT}\right], \quad (2.2)$$

where E_F is Fermi energy with respect to the bottom of the conduction-band (E_c) and the top of the valence-band (E_v), k is the Boltzmann's constant and T is the temperature.

At thermal-equilibrium, concentration of holes in the valence band can be described by

$$p_0 = \int g_v(E)[1-f_F(E)] dE, \quad (2.3)$$

where p_0 is the thermal-equilibrium concentration of hole, $g_v(E)$ is the density of states in the valence band. For energy states in the valence band, the Boltzmann approximation becomes

$$1-f_F(E) = \frac{1}{1 + \exp\left(\frac{E_F - E}{kT}\right)} \approx \exp\left[\frac{-(E_F - E)}{kT}\right]. \quad (2.4)$$

Briefly, the thermal-equilibrium concentrations of electron and hole can be written as

$$n_0 = N_c \exp\left[\frac{-(E_c - E_F)}{kT}\right], \quad (2.5)$$

$$p_0 = N_v \exp\left[\frac{-(E_F - E_v)}{kT}\right]. \quad (2.6)$$

N_c and N_v parameters are called the effective density of states function in the conduction band and valence band, respectively. The magnitude of N_c and N_v is generally on the order of 10^{19} cm^{-3} at $T = 300 \text{ K}$ for most semiconductors.

Because, the concentration of electrons in the conduction band equal to the concentration of hole in the valence band. It may be denoted n_i and p_i as the electron and hole concentrations. Therefore, one can simply use the parameter n_i as the intrinsic carrier concentration, that refers to either the intrinsic electron or hole concentrations. By taking the product of Eq.(2.5) and Eq.(2.6),

$$n_i^2 = N_c N_v \exp\left[\frac{-(E_c - E_v)}{kT}\right] = N_c N_v \exp\left[\frac{-E_g}{kT}\right], \quad (2.7)$$

where E_g is the bandgap energy.

However, the intrinsic semiconductor is seen an interesting material for many applications, the important role of semiconductor is realized by adding small, controlled amounts of specific dopant or impurity atoms. The doped semiconductor is called an “extrinsic semiconductor” which can extremely alter the electrical characteristics of the semiconductor. Naturally, semiconductors

are formed by covalent bonding. But when group V element such as phosphorus is added, it acts as a substitutional impurity. The group V elements have five electrons, four of them form the covalent bonding with the silicon atoms, leaving the fifth valence electron of phosphorus atom. It is called a donor electron as shown in Fig.6(a). The other energy state within the forbidden band is called as “donor energy” as shown in Fig.6(b). If an amount of energy, such as thermal energy, is added to the donor electrons which place in the donor energy state, it will be elevated into the conduction band and leaving behind a phosphorus positive charge which is fixed. Finally, a current can be generated by electron moving in the conduction band through the crystal. This effect means that the donor impurity atoms add electron to the conduction band without creating hole in the valence band, this kind of material is called “n-type semiconductor”.

On the other hand, “p-type semiconductor” is the case when adding group III elements with three valence electrons, such as Boron, and it acts as a substitutional impurity to silicon. These three valence electrons are taken up in the covalent bonding as shown in Fig.7(a). One covalent bonding position appears to be empty, and the Boron atom becomes “acceptor impurity atom”. The acceptor energy state will be created where it is located close to the valence band as shown in Fig.7(b). Its energy is far smaller than conduction band energy. The empty state in the acceptor energy state will be occupied by valence electrons in valence band. When it has a small amount of thermal energy, the vacant electron positions in valence band can be thought of as holes. So, the acceptor atoms can generate holes in the valence band without generating electron in the conduction band.

Both of n- and p-types semiconductors can also be basically described in the thermal-equilibrium concentration of electron and hole by applying Eq.(2.5) and (2.6),

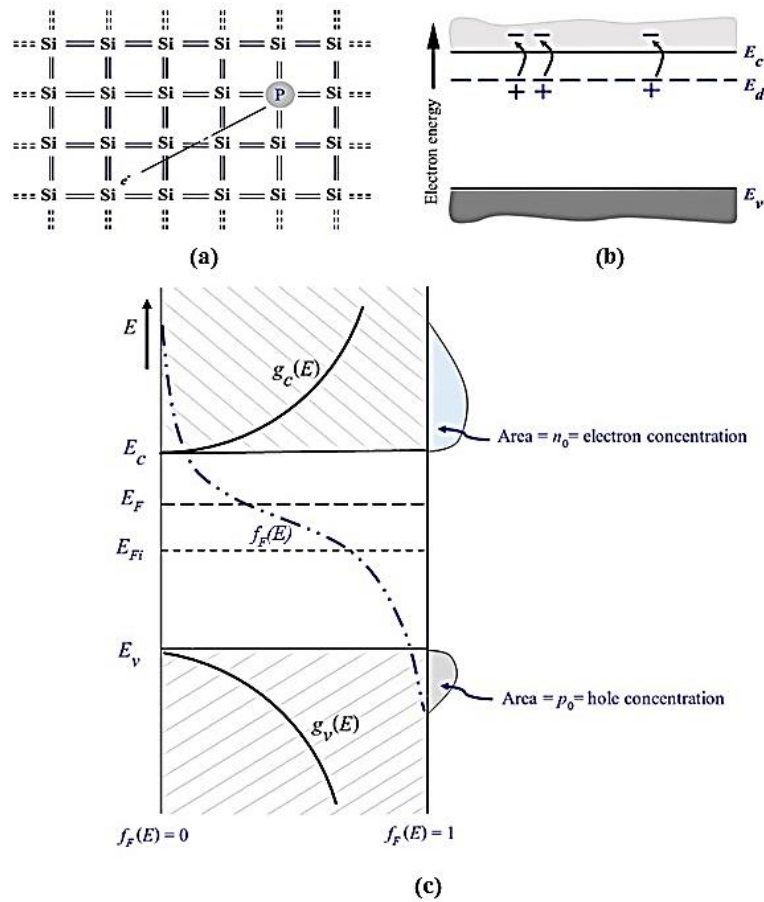


Figure 6 (a) Two-dimensional representation of the silicon lattice doped with a phosphorus atom; (b) The energy-band diagram showing the effect of a donor state being ionized; (c) Density of states functions, Fermi-Dirac probability function, and areas representing electron and hole concentration for the case when E_F is above the intrinsic Fermi energy [24].

$$n_0 = n_i \exp\left[\frac{E_F - E_{Fi}}{kT}\right], \quad (2.8)$$

$$p_0 = n_i \exp\left[\frac{-(E_F - E_{Fi})}{kT}\right]. \quad (2.9)$$

Eq.(2.8) and Eq.(2.9) show that the Fermi energy level changes from the intrinsic Fermi level. In case of a n-type, $E_F > E_{Fi}$. Then $n_0 > p_0$ and the probability function in conduction band increases. Similarly, in a p-type case, $E_F < E_{Fi}$ so that

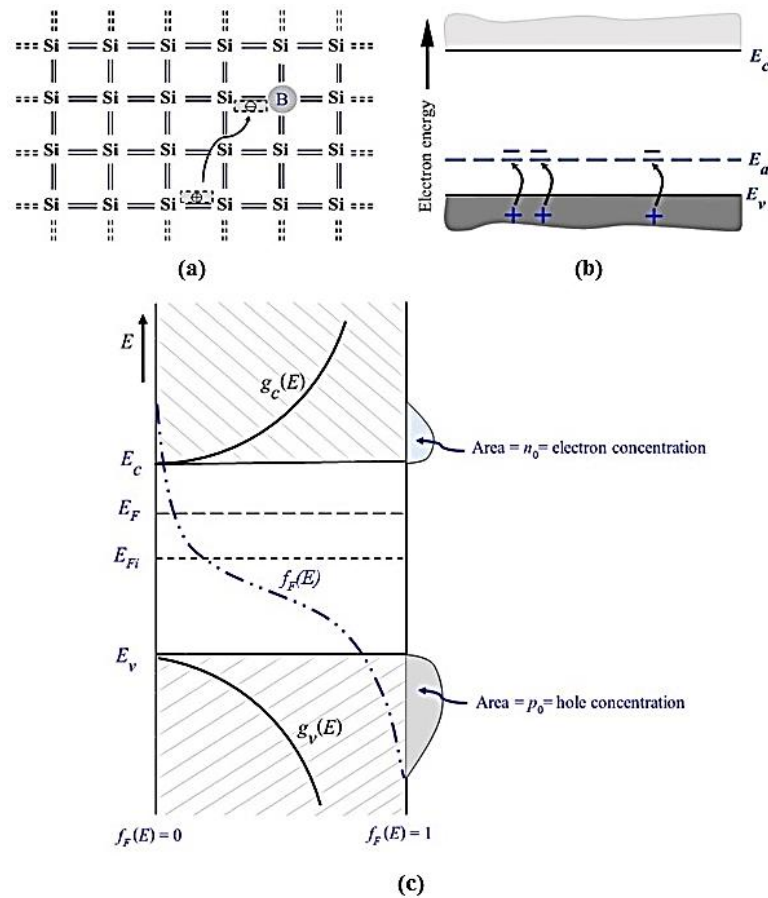


Figure 7 (a) Two-dimensional representation of the silicon lattice showing the ionization of the boron atom resulting in a hole; (b) The energy-band diagram showing the effect of an acceptor state being ionized; (c) Density of states functions, Fermi-Dirac probability function, and areas representing electron and hole concentration for the case when E_F is below the intrinsic Fermi energy [24].

$p_0 > n_0$ and the probability, $1 - f_F(E)$, of an empty state (hole) in valence band decreases.

2.1.2 Principles of Solar Cells

A solar cell is a p-n junction device with no voltage directly applied across the junction. It converts photo power into electrical power and delivers this power to an external load.

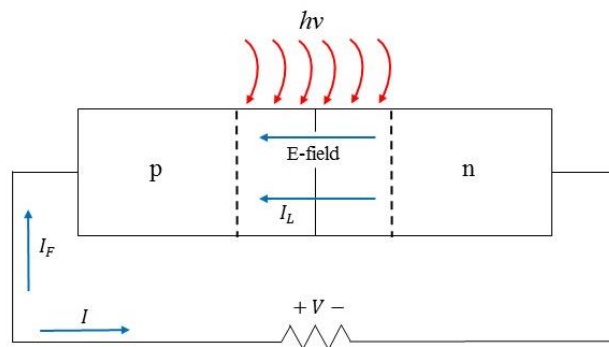


Figure 8 A p-n junction solar cell with resistive load.

Consider the p-n junction with a resistive load. Even the zero bias applied to the junction, an electric field exists in the space charge region as shown in Fig.8. Incident photon illumination can create electron-hole pairs in the space charge region that will be swept out producing the photocurrent I_L in the reverse-biased direction. I_L produces a voltage drop across the resistive load which forward biases the p-n junction. The forward-bias voltage produces a forward-bias current, I_F . The net p-n junction current in the reverse-biased direction is

$$I = I_L - I_F = I_L - I_S \left[\exp\left(\frac{eV}{kT}\right) - 1 \right], \quad (2.10)$$

where the ideal diode equation has been used. The I_S is the device saturation current. The photocurrent and the net solar cell current are always in the reverse-biased direction.

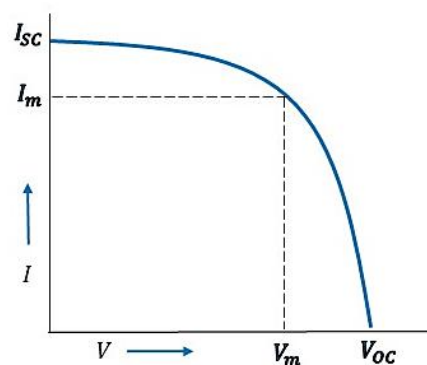


Figure 9 I-V characteristics of a p-n junction solar cell.

A plot of the diode current (I) as a function of the diode voltage (V) from Eq.(2.10) is shown in Fig.9. Interestingly, the short-circuit condition occurs when the resistance is zero so that voltage becomes zero. The current in this case is referred to as the short-circuit current, or

$$I = I_{sc} = I_L . \quad (2.11)$$

The open-circuit condition occurs when the resistance is very large. The net current is zero and the produced voltage is the open-circuit voltage. The photocurrent is now balanced by the forward-biased junction current,

$$I = 0 = I_L - I_S \left[\exp\left(\frac{eV}{kT}\right) - 1 \right] . \quad (2.12)$$

The open circuit voltage V_{oc} can be defined as

$$V_{oc} = V_t \ln\left(1 + \frac{I_L}{I_S}\right) , \quad (2.13)$$

where V_t is the total voltage. The power delivers to the load is

$$P = I \cdot V = I_L \cdot V - I_S \left[\exp\left(\frac{eV}{kT}\right) - 1 \right] \cdot V . \quad (2.14)$$

The conversion efficiency of a solar cell is defined as the ratio of output electrical power to incident optical power (P_{in}). For the maximum power output (P_m), it can be written as

$$\eta = \frac{P_m}{P_{in}} \times 100\% = \frac{I_m V_m}{I_{sc} V_{oc}} \times 100\% . \quad (2.15)$$

Thus, the maximum possible current and the maximum possible voltage are I_{sc} and V_{oc} , respectively. The ratio of $I_m V_m / I_{sc} V_{oc}$ is called the fill factor which is a measure of the realizable power from a solar cell. The fill factor of a good device is typically between 0.7 and 0.8 [24].

2.2 $\text{CuIn}_{1-x}\text{Ga}_x\text{Se}_2$

2.2.1 Fundamental properties

The CuInSe_2 and CuGaSe_2 materials have the chalcopyrite structure as shown in Fig 10. They are ternary compound I-III-VI₂ semiconductor. Group I is Cu, Ag, and Au. Group III is Al, In, and Ga. Group VI consists of S, Se, and Te. It forms a tetragonal unit cell with a ratio of the lattice parameters c/a approximately close to 2. The deviation of those lattice parameter is called the tetragonal distortion due to different strength of the Cu-Se and the In-Se or Ga-Se bonds.

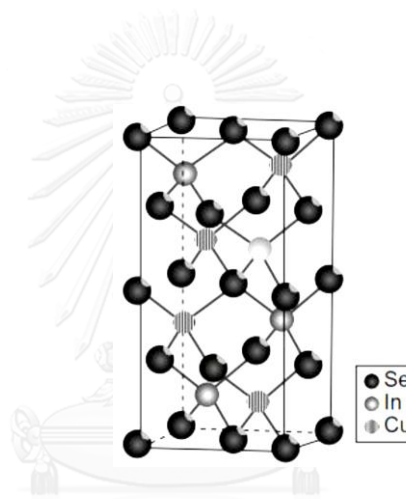


Figure 10 The unit cell of the chalcopyrite structure [9].

The possible phases in the Cu-In-Se system are graphically described in Fig.11. The CIGS thin film is prepared under an excess supply of Se. It has compositions that fall on, or close to the tie-line between Cu_2Se and In_2Se_3 . The chalcopyrite phase of CuInSe_2 is located on this line. The details of the Cu_2Se - In_2Se_3 tie-line near CuInSe_2 are briefly described by the pseudo-binary phase diagram that shows in Fig.12. Above 500 °C, it widens towards the In-rich side. Typically, the average composition of films is about 22 to 24 at. % of Cu [9].

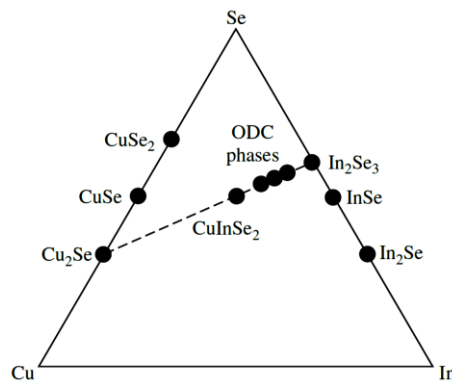


Figure 11 Ternary phase diagram of the Cu-In-Se system. Thin-film composition is usually near the pseudo-binary Cu_2Se - In_2Se_3 tie line [9].

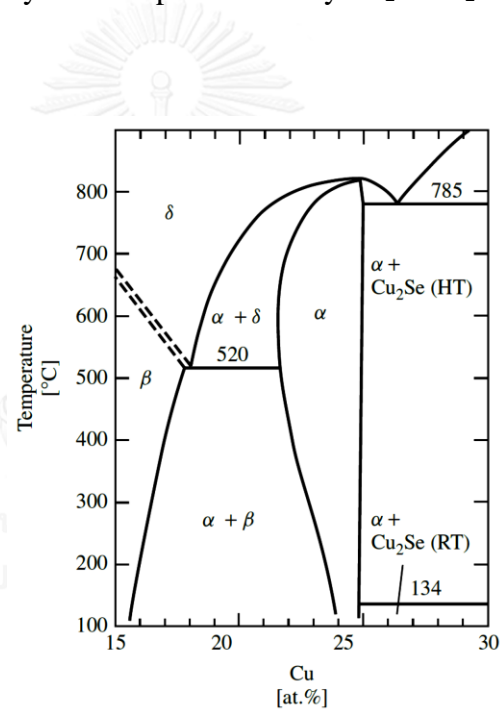


Figure 12 Pseudo-binary In_2Se_3 - Cu_2Se equilibrium phase diagram for compositions around the CuInSe_2 chalcopyrite phase (α). The δ phase is the high-temperature sphalerite phase, and the β is as ordered defect phase (ODC). Cu_2Se exists as a room-temperature (RT) or high-temperature (HT) phase [9].

CuInSe_2 can be alloyed in any proportion with CuGaSe_2 , leading to form $\text{Cu}(\text{In,Ga})\text{Se}_2$. In the same way, In_2Se_3 phase at the end point of the pseudo-binary tie-line can also be allowed to form $(\text{In,Ga})_2\text{Se}_3$. Thus, it has a band gap

energy in range of 1.04 - 1.68 eV depending on Ga concentration. The CIGS solar cell with high performance can be fabricated with $x = [\text{Ga}]/([\text{Ga}]+[\text{In}])$ ratio ranges 0.2 to 0.3 and 0.7 to nearly 1 for $y = [\text{Cu}]/([\text{Ga}]+[\text{In}])$ ratio. Also, the band gap energy of 1.2 - 1.3 eV is desirable for the high efficiency solar cells [9].

There are important reasons that CIGS material was chosen for a solar cell. One reason is a high absorption coefficient among several semiconducting materials for solar cell application such as InP, CdTe, GaAs, a-Si, and c-Si. The relationship between absorption coefficients (cm^{-1}) and photon energy (eV) of those materials is shown in Fig.13. The other reason comes from the limit for the efficiency of solar cell as shown in Fig.14. It known as Shockley-Queisser limit (SQ limit) that demonstrates the maximum theoretical efficiency of a solar cell using a single p-n junction device to collect power from the cell. The SQ limit indicates that CIGS material has potential to produce high efficiency which the maximum efficiency can increase up to about 30% [25].

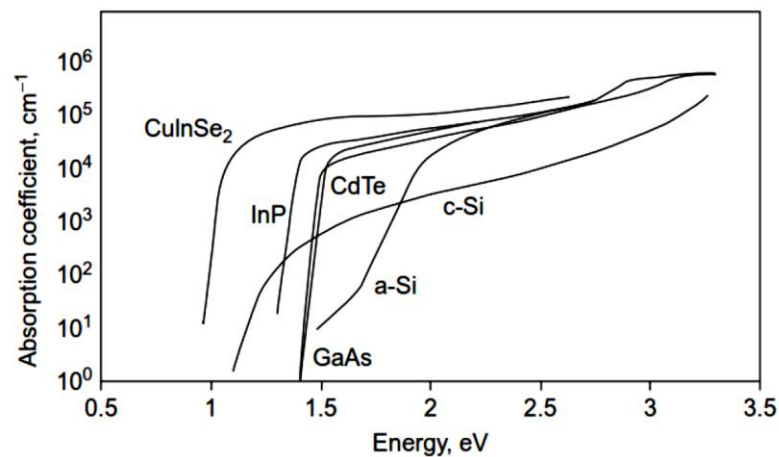


Figure 13 Absorption coefficient versus photon energy of various semiconducting materials [25].

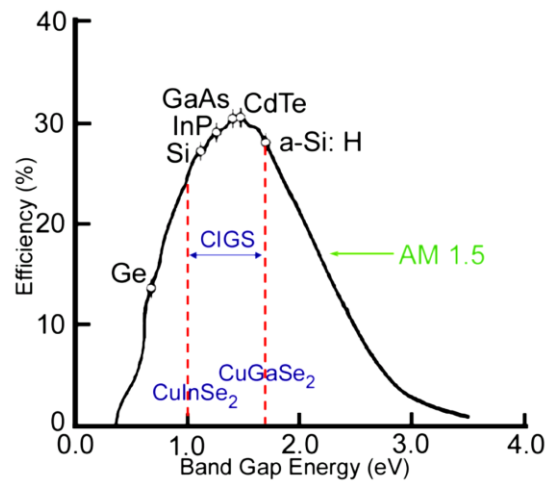


Figure 14 The theoretical efficiencies of various solar cell materials [25].

2.2.2 $\text{CuIn}_{1-x}\text{Ga}_x\text{Se}_2$ based-thin film solar cells

The first CIGS solar cell started in 1975 when Bell laboratory scientists achieved a 12% solar cell conversion efficiency by evaporating n-type CdS onto p-type CuInSe_2 single crystal. In the early 1985s, Boeing introduced a co-evaporation process where Cu, In, and Se were deposited from separating evaporation sources and achieved a more than 10% efficiency. Then, Arco Solar Cell demonstrated a deposition-reaction process using Cu and In metallic precursors, with H_2Se as the reacting chalcogen source that gave better device efficiency than the co-evaporation. In fact, a CIGS absorber layer was doped with Na during the deposition-reaction process. In 1995, Na-containing glasses became standard technique in co-evaporation as well. Both of them reached almost similar efficiency of around 14%. However, a more efficient growth technique belongs to co-evaporation which employed more complicated evaporation processes. The so-called three-stage process was invented in 1994 by NREL group. They achieved an efficiency of 20%. Six years later, Wuerth Solar brought the co-evaporation into commercial production. They designed line-evaporation sources that were able to deposit on 2 ft-wide substrate. Such both processes are still in competition and may further be pursued in parallel. Nowadays, several laboratories around the world had the experience to prepare a CIGS solar cell with an above 19% efficiency [9]. In 2015, Solar Frontier

achieved an efficiency of 22.3% by co-evaporation [26]. Now, P. Jackson *et. al.* presently reached an efficiency up to 22.6% by using alkali post deposition treatment (PDT) [27].

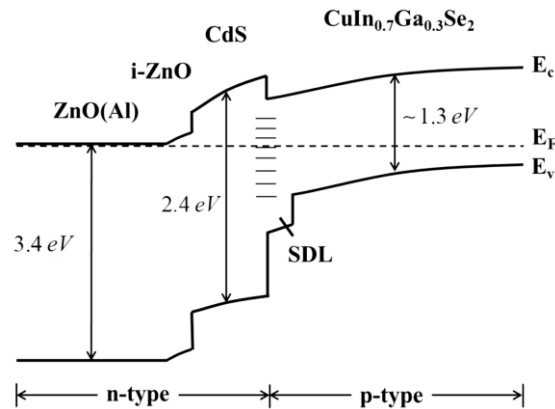


Figure 15 One-dimensional energy band diagram of the ZnO/CdS/CIGS heterojunction showing p-n junction and surface defect layer (SDL) together with inter recombination center at the CdS/CIGS interface [25].

The typical structure of the CIGS solar cell consists of multi-layers of semiconducting materials with different band gaps to form a p-n junction. There are many materials used as a bottom substrate including glass, metal, and polymer. Soda-lime glass (SLG) is extensively used as a substrate. A CIGS layer is deposited on SLG coated with molybdenum. Then, a thin i-CdS layer is required as a buffer layer, and n-ZnO will be deposited as a window layer. There are three possible junction models such as the p-CIGS/n-CdS heterojunction, p-CIGS/n-CIGS homojunction and p-CIGS/n-ordered defect compound (ODC) layer heterojunction [28]. The first one is the most widely accepted where the p-n junction is naturally formed at the interface between the two different materials, CIGS and CdS. The typical energy band alignment of CIGS thin film solar cell can be seen in Fig.15.

2.3 The Multi-Source Co-Evaporation

2.3.1 Multi-Source Co-Evaporation System

The CIGS thin films are grown on the Mo/SLG substrates by multi-source co-evaporation system with the base pressure of about 10^{-6} Torr when the source materials are not heated. The pure elements (Cu, In, Ga, and Se) are evaporated from four Knudsen-type sources or effusion cells (K-cell). The source crucibles are made of pyrolytic boron nitride (PBN) which are heated by heater filaments. These four crucibles are mounted on the baseplate at the bottom of the chamber. Typically, the four evaporation sources are independently controlled by programmable PID temperature controllers. A Mo-coated SLG (2 mm thick with the area of $10\text{ cm} \times 10\text{ cm}$) substrate positioned approximately 25 cm above the sources is heated by radiation from the heater. The heater temperature (T_{heater}) is controlled and kept constant by regulating the output power (OP) of the controller. The radiation from the front surface of the substrate is monitored by a high-resolution monochromatic (InGaAs, $1.55\text{ }\mu\text{m}$) pyrometer. The pyrometer is focused to the center of the substrate surface by the built-in laser guided device. The growth system is shown in Fig.16. During the process (almost 120 minutes), the substrate temperature (T_{sub}), heating OP (%OP) and temperature of the CIGS surface (T_{pyro}) are monitored simultaneously which is shown as an example of growth profile in Fig.17.

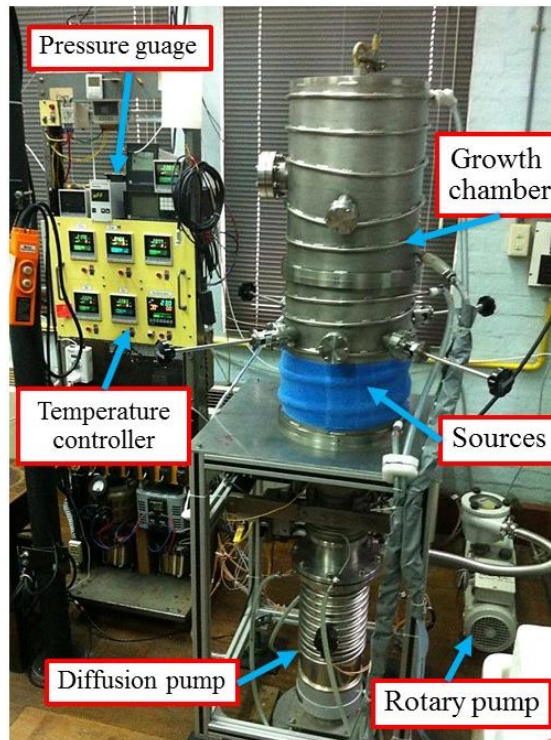


Figure 16 The multi-source co-evaporation system with the in situ monitoring.

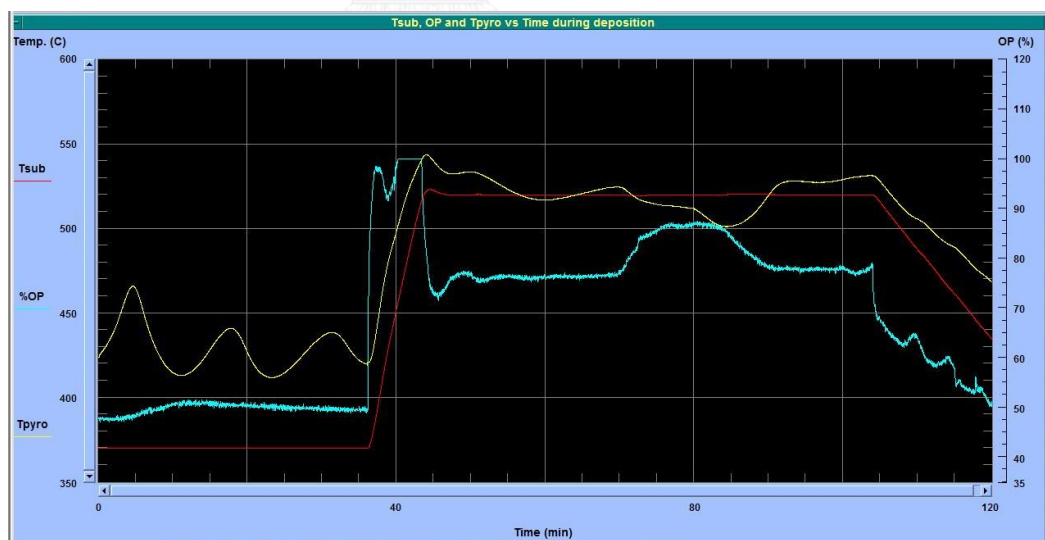


Figure 17 The example growth profile in a display monitor from co-evaporation system, e.g. three-stage process.

2.3.2 Three-Stage Co-Evaporation

The three-stage co-evaporation from elemental sources in the presence of excess Se vapour is the most successful CIGS absorber deposition method for high efficiency and small-area devices [29]. The three-stage process is a sequential process in which In and Ga are evaporated separately from the Cu. It was firstly introduced by the deposition of an $(\text{In,Ga})_x\text{Se}_y$ compound, followed by the deposition of Cu and Se until the film reaches the desired composition [30], [31]. So, this process is to create the inter-diffuse layers to form the CIGS film. The other attempt allows the Cu delivery to continue until the film becomes an overall Cu-rich composition [32]. For third stage, bring the composition back to slightly Cu-deficient by evaporating In and Ga, again in the presence of excess Se. Then, the as-grown film forms the ternary chalcopyrite film. The deposition rate, substrate temperature, and film composition profiles can be schematically describes in Fig.18 and 19.

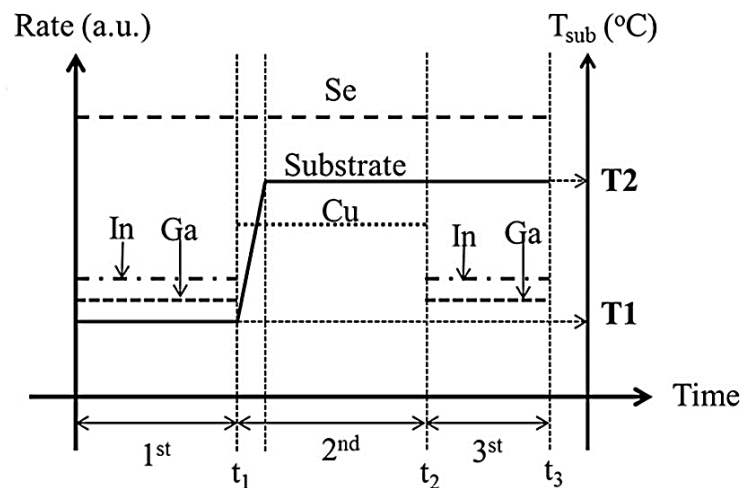


Figure 18 Metal fluxes of three-stage process used to fabricate the CIGS film, including the substrate temperature profile used during the film growth.

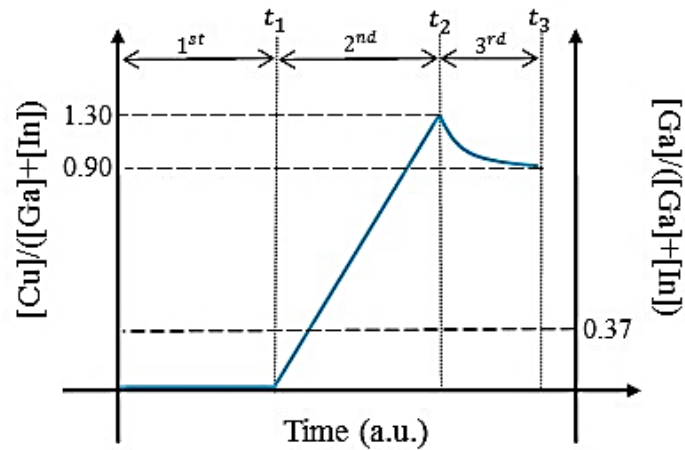


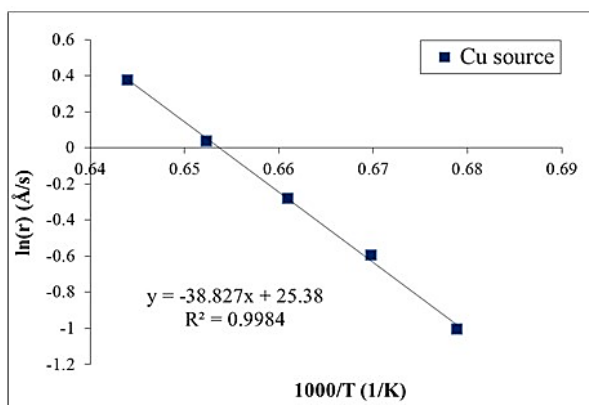
Figure 19 The CIGS thin film compositions profile in three-stage process.

2.3.3 Calculation of the CIGS deposition rate

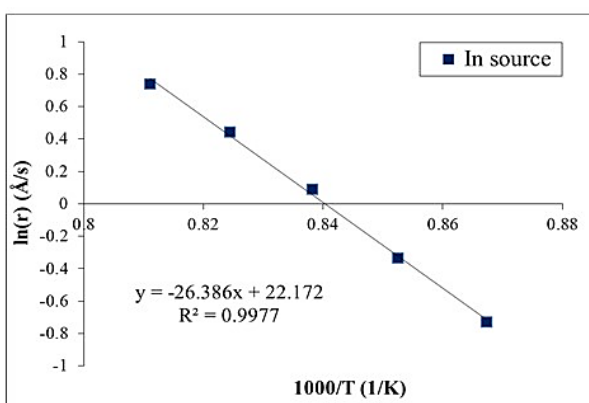
Normally, before the beginning of the three-stage co-evaporation method, it is needed to find the suitable effusion cell temperatures. First, it begins by setting the x and y values. The relationship between the deposition rate and the effusion cell temperature is given by

$$\ln(r) = \frac{a}{T} + b, \quad (2.16)$$

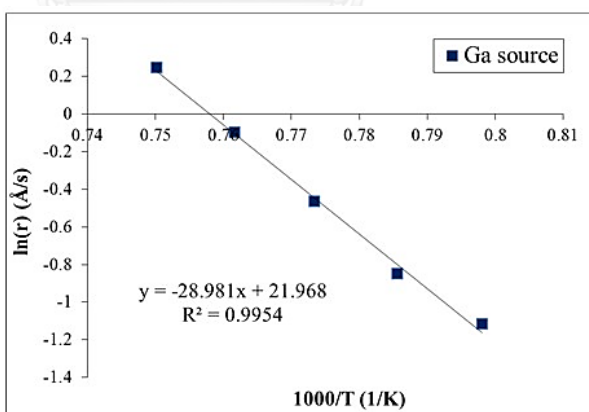
where r is the deposition rate ($\text{\AA}/\text{s}$), T is the effusion cell temperature ($^{\circ}\text{C}$). The values of parameters a and b for each sources are from fitting the data with the least-square method. The example of the evaporation rate with temperature of each elemental source are shown in Fig.20.



(a)



(b)



(c)

Figure 20 The graphs of evaporation rate obtained by the QCM versus elemental temperature of (a) Cu, (b) In and (c) Ga sources to obtain the parameters a and b by least-square fitting.

Therefore, the deposition rates of elemental sources must be defined at first, especially the deposition rate of Cu source that depends on the required thickness of CIGS film as shown in Eq. (2.17) and (2.18)

$$r_{\text{Cu}} = \frac{d_{\text{Cu}}}{t_{\text{Cu}}}, \quad (2.17)$$

where r_{Cu} is the deposition rate of Cu ($\text{\AA}/\text{s}$), d_{Cu} is the thickness of Cu (\AA), and t_{Cu} is the deposition time of Cu (s). Due to the $\text{CuIn}_{1-x}\text{Ga}_x\text{Se}_2$ (CIGS) layer is an alloy of two compounds, CuInSe_2 (CIS; $x=0$) and CuGaSe_2 (CGS; $x=1$). The values of density (ρ) and molecular mass (M) are function of x , and the ratio of N_{Cu} and N_{CIGS} is equal to unity.

$$\begin{aligned} \frac{d_{\text{Cu}}}{d_{\text{CIGS}}} &= \frac{N_{\text{Cu}} \cdot M_{\text{Cu}}}{\rho_{\text{Cu}}} \bigg/ \frac{N_{\text{CIGS}} \cdot M_{\text{CIGS}}}{\rho_{\text{CIGS}}} \\ &= \frac{N_{\text{Cu}} \cdot M_{\text{Cu}} \cdot [\rho_{\text{CIS}} \cdot (1-x) + \rho_{\text{CGS}} \cdot x]}{N_{\text{CIGS}} \cdot [M_{\text{Cu}} + M_{\text{In}} \cdot (1-x) + M_{\text{Ga}} \cdot x + 2M_{\text{Se}}] \cdot \rho_{\text{Cu}}}. \end{aligned} \quad (2.18)$$

Given N_{Cu} is the number of Cu atoms, N_{CIGS} is the number of CIGS molecules, ρ_i is the density of element i , and M_i is the molecular mass of element i .

The rate of Ga (r_{Ga}) and In (r_{In}) can be calculated from

$$r_{\text{Ga}} = \frac{x}{y} \cdot \frac{\alpha_{\text{Cu}}}{\alpha_{\text{Ga}}} \cdot r_{\text{Cu}}, \quad (2.19)$$

and

$$r_{\text{In}} = \frac{(1-x)}{y} \cdot \frac{\alpha_{\text{Cu}}}{\alpha_{\text{In}}} \cdot r_{\text{Cu}}, \quad (2.20)$$

where x is the ratio of Ga to group III elements $\text{Ga}/(\text{Ga}+\text{In})$ and y is the ratio of Cu to group III elements $\text{Cu}/(\text{Ga}+\text{In})$.

The parameter α is defined as the ratio of the ρ_i to the M_i of each elements that it shown in Table 1.

$$\alpha_{\text{Cu}} = \rho_{\text{Cu}} \cdot M_{\text{Cu}}^{-1} = 0.1410 \text{ (mol/cm}^3\text{)}, \quad (2.21)$$

$$\alpha_{\text{Ga}} = \rho_{\text{Ga}} \cdot M_{\text{Ga}}^{-1} = 0.0848 \text{ (mol/cm}^3\text{)}, \quad (2.22)$$

and
$$\alpha_{\text{In}} = \rho_{\text{In}} \cdot M_{\text{In}}^{-1} = 0.0637 \text{ (mol/cm}^3\text{)}. \quad (2.23)$$

Substitution of r_{Cu} , r_{In} , and r_{Ga} into Eq. (2.16) as well as parameters a and b from obtained from the least square fitting of the data shown in the graphs of Fig.20, the working temperature of each element will be achieved. The details for the CIGS thin film fabrication in this work are described in the chapter 3.

Table 1 Density and molecular mass of the material used in CIGS fabrication process [33].

Material	$\rho_i \text{ (g/cm}^3\text{)}$	M (g/mol)
Cu	8.96	63.55
In	7.31	114.82
Ga	5.91	69.72
Se	4.79	78.96
CIS	5.89	336.29
CGS	5.27	291.19

2.4 Chemical Etching Processes

2.4.1 Wet-etching method

Indeed, there are two main etching methods such as wet etching and dry etching. The applications of various chemical types are described in Table.2. The wet chemical etching (WCE) or liquid solution etching is involved in the development or fabrication of any metal or metallic compounds, which it is used process in this study. A material can be typically immersed in a chemical bath. Wet chemical etchants are usually isotropic etching, leading to large bias when etching thick films. A major factor in chemical processing involves the physical structure of the material on which it is applied. There are a number of different applications such as removal, polishing, preferential, and structuring, etc. Water is the primary diluent for solution reactivity control. Also, both alcohol and

solvents are similarly used as well as other acids as buffering agents. About the surface oxidation, it can be a major concern in chemical processing that all metal and metallic compounds always have a native oxide on their surfaces. Such oxides are considered as surface contamination. There are oils, greases, dirt or other organic residues. The contamination directly alter both physical and electrical parameters. The individual metal and metallic layers may require a specifically designed solution in order to characterize the physical properties. The etching rates on concave and convex surfaces become a key factor for some special forming or fabricating methods.

Table 2 The applications of each chemical types [15].

Chemical type	Application
Acid	Cleaning, polish
Alkali	Damage removal, polishing, jet
Alcohol	Dislocation, preferential
Gas	Isotropic, oxide etch
Halogen	Anisotropic, oxide removal
Ionic gas	Junction, selective
Metal	Macro-etch, sphere
Molten flux	Micro-etch, structure
Salt	Mesa, stain
Solvent	Orientation, step
Electrolytic	Forming, thinning

In acid etch method, almost all known inorganic solids, whether they are an element, natural mineral or an artificially grown material can be etched in either a single acid or acid mixture. The material solubility is controlled by concentration with dilution usually by water or solution temperature. Semiconductors and many metal compounds require mixed acid to produce an oxidation-reduction reaction. Most acids are obtained and used in liquid form as a specific concentration in water. Also, it can be used in several physical ways including immersion, jet, spray, hot vapor, etc., and for specific results such as cleaning, polishing, surface structuring, defect development, or thinning.



For alkali etch or base etch method, it is a solution with pH greater than 7. They may be in liquid form such as ammonium hydroxide (NH_4OH) or in solid form as potassium hydroxide (KOH) and sodium hydroxide (NaOH). The solid hydroxide must be dissolved in water or alcohol for a specific concentration. The term “hydroxide” is often used in place of alkali or base. Generally, hydroxides are weak etch at room temperature and primarily used for surface cleaning in concentration of 2 to 15%. The concentration between 20 to 50% with heating to boiling, they act as removal etchants, surface preferential, and also developing crystallographic structure. Also, alkali can be used as molten fluxes for preferential etching such as on silicon [15].

CHAPTER III

EXPERIMENTAL PROCEDURES

In this chapter, the fabrication of the CIGS solar cell will be described at first. Especially, the three-stage co-evaporation is used to grow the CIGS thin film by fixed x- and y-values. Also, the details of growth profile and monitoring system in three-stage process will be explained. Then, the wet-etching method will be introduced to alter the CIGS surface in order to vary the surface roughness. The characterizations of thin film solar cells will be discussed such as field-emission scanning electron microscopy (FESEM), atomic force microscopy (AFM), current-voltage (I-V) measurement, and external quantum efficiency (EQE) measurement.

3.1 CIGS Solar Cell Fabrication

3.1.1 Substrate preparation

Soda-lime glass (SLG) is used as a substrate in this research. It is 10 cm × 10 cm and 2 mm thick. Before the deposition of the molybdenum back contact, the substrates must be cleaned. It is the first important step in solar cell fabrication. Because the various contaminations on the SLG surface can influence to a loss of adhesion that becomes an unknown defect in the film. First, it is rubbed with a soapy cellulose sponge. Then, it is put in an ultrasonic bath with deionized (DI) water. Next, it is immersed into a tank with DI-water and Micro-90 detergent. The tank is heated to 60 °C and, subsequently, put into an ultrasonic bath for 1 hr. After that, a rinsing step in 60 °C DI-water using ultrasonic bath is required and followed by soaking into Chromic acid (H₂CrO₄) bath for 1 hr. Finally, the substrates are rinsed and dried by DI-water again and nitrogen gas, respectively.

3.1.2 Mo back contact

There are many reasons to choose molybdenum (Mo) as a back contact of CIGS solar cell. First, Mo has a high melting temperature about 2,623 °C, and it does not degrade during CIGS growth process. Second, Mo is an Ohmic contact with CIGS material. It can react with selenium to form MoSe₂ interface layer at high temperature about 600 °C. Third, it has a good adhesion property to the SLG substrate with suitable thermal expansion between the Mo film and the SLG substrate. Lastly, it has a low resistivity contact and especially has cost effectiveness [9].

In this research, the Mo back contact layer is deposited by a dc sputtering technique using a Mo target with 99.95% purity. The substrate to target distance is about 6 cm. The sputtering pressure and power are about 3.0×10^{-6} mbar and 550 W, respectively. The Ar gas flows during sputtering is 23.0 sccm. The substrate holder passes in front of the Mo-target with a speed of 3 rpm for the relaxation of the Mo film during the deposition process. With 12 min of sputtering time, 600 nm thick of Mo layer is obtained.

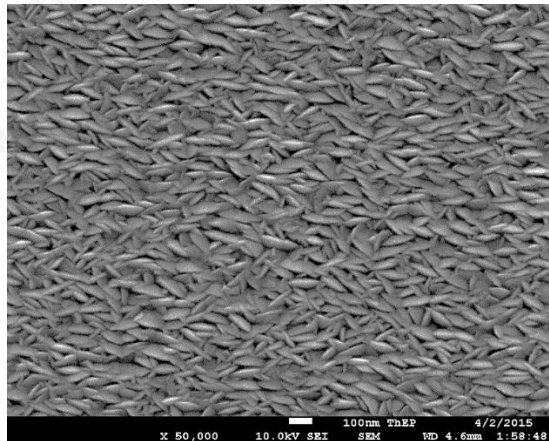


Figure 21 The FESEM image of as-grown Mo surface.

3.1.3 CIGS absorber

A CIGS thin films is grown by the three-stage co-evaporation technique. A 10 cm × 10 cm Mo/SLG substrate is mounted into metal frame at the top of

the deposition chamber. A flux of Se at 290 °C is evaporated in excess amount throughout the evaporating duration. In first stage, the substrate is heated to 370 °C from the backside by means of heater delivering constant power. In, Ga, and Se are co-evaporated to form $(\text{In,Ga})_2\text{Se}_3$ precursor. In the second stage, the substrate is then heated up to 560 °C in a flux of Cu and Se. Enough Cu is added to achieve the overall composition Cu-rich ($y > 1$). Lastly, in a third stage, In, Ga, and Se are co-evaporated to bring the overall composition back into slightly Cu-poor regime ($y \sim 0.9$). By observing variation of T_{pyro} , T_{sub} , and %OP, the desired final Cu-deficient composition (end point detection or EPD) of the film can be obtained. The amount of In and Ga in the third stage is around 10% of the total in the first and third stages. The sample is then cooled down in a flux of Se for about 30 min. The total CIGS film thickness is approximately about 1.8 μm . $[\text{Cu}]/([\text{Ga}]+[\text{In}])$ and $[\text{Ga}]/([\text{Ga}]+[\text{In}])$ ratios are set to achieve 0.90 and 0.37, respectively. The compositions of the as-grown CIGS film are measured in order to verify $[\text{Cu}]/([\text{Ga}]+[\text{In}])$ and $[\text{Ga}]/([\text{Ga}]+[\text{In}])$ ratios by energy dispersive x-ray spectroscopy (EDS). Finally, the samples are delicately cut into nine pieces of 3 cm \times 3 cm before the deposition of CdS.

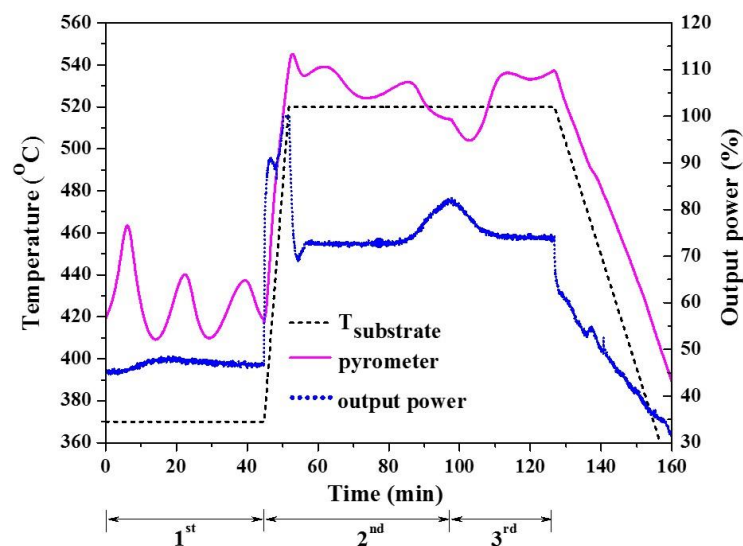


Figure 22 Temperature profile for the three-stage co-evaporation of CIGS thin film.

As mentioned above, in order to control a phase transition from Cu-rich to Cu-poor film, the *in situ* monitoring signals of substrate heating power and pyrometer are used to control the growth process. The main principle of CIGS film monitoring is based on the different emissivity of the change in $[Cu]/([Ga]+[In])$ ratio or y -value, including Cu_xSe , stoichiometric, and also Cu-poor CIGS compounds. In Fig.22, it evidently shows that the monitoring signal is sensitive to the phase change. For pyrometer measurement, it measures the temperature of CIGS surface by observing irradiation of photon at wavelength $1.55 \mu m$. The periods of oscillations in the pyrometer signal can be used to verify the deposition rate of the film. The damping of the oscillation amplitude occurs probably due to the increasing of absorption in the band gap and also the increasing roughness of reflecting surface. In addition, a reproducible co-evaporation method requires good control of the elemental fluxes from each evaporating sources. The evaporation rates from each sources can be simply controlled by the source temperatures.

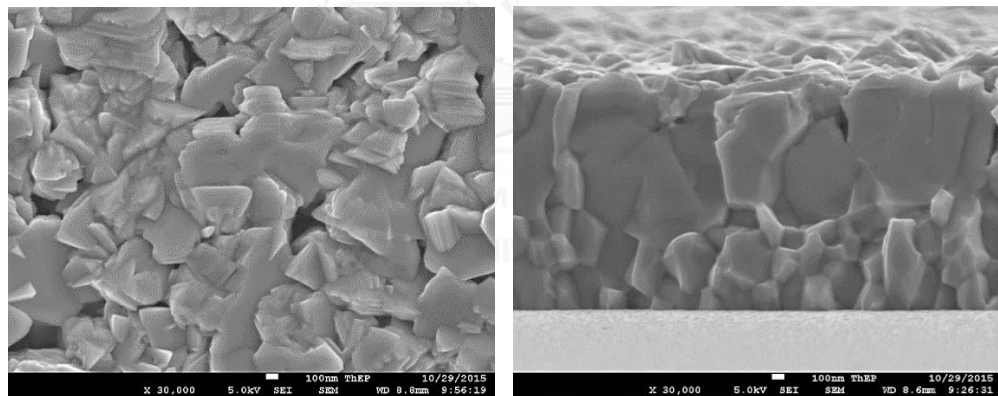


Figure 23 The FESEM images of as-grown CIGS surface (left) and cross-sectional view (right).

3.1.4 CdS buffer

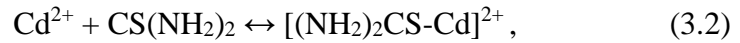
Cadmium sulfide (CdS) is a popular buffer layer which acts as a protecting layer between the CIGS absorber and the window layers. The benefits of a buffer layer is to protect the CIGS surface during the sputtering of i -ZnO, ZnO(Al), and intercept the diffusion of Zn into the CIGS layer. There

are many methods to deposit CdS such as chemical bath deposition (CBD) and sputtering techniques. The CBD method is usually preferred for CdS deposition which can achieve higher CIGS solar cell performance than sputtering technique. The CBD helps to clean or remove native oxides on CIGS surface before growing CdS. Naturally, the reaction in CdS-CBD is ion by ion mechanism or by clustering of colloidal particles. It may form cubic, hexagonal, or a mixture of CdS lattice structure [9]. Moreover, an ion by ion mechanism can result in dense homogeneous CdS films with mixed cubic/hexagonal or predominantly hexagonal lattice structure. The significant issues at CIGS/CdS interface mainly come from the CBD process that shows a small electron barrier in conduction band and stoichiometric CdS are formed while the CdS-sputtering technique shows the Cu and Cd intermixing interface and S-rich CdS film [8].

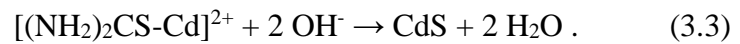
In our CdS deposition steps, a CdS buffer layer by a standard CBD process is followed after the CIGS process. It is deposited as soon as possible after the samples are brought out in open air, normally within 5 min. This is done to minimize oxidation and other reactions of the CIGS layer that begins to occur as soon as it is exposed to air. The impurities at CdS/CIGS interface relate to a reduction of the electronic structure. The CBD bath contains a solution with 80 ml of ammonia solution 25% (NH₃), 0.37 M of thiourea (SC(NH₂)₂), and 0.03 M of cadmium sulfate (CdSO₄). The solution is mixed in a beaker at room temperature, and the as-grown CIGS is immersed into the beaker, which is constantly heated at 65 °C in a water bath. During the CBD process (15 min), the solution is stirred by magnetic bar with 150 rpm. In particular, native oxides are removed by the ammonia [9]. Then, it is immersed and rinsed into a beaker with DI-water to stop the growth process. Finally, it is dried with a nitrogen gas. This process yields about 50-100 nm thick of CdS layer. The chemical reaction mechanism of CdS deposition is explained by starting with the ionization of CdSO₄, it is called the dissociation of complex to free Cd²⁺ ion.



Consider the complexation of free Cd^{2+} by thiourea to give a Cd-thiourea complexation.



Then, the Cd-thiourea ion could hydrolyze by breaking the S-C bond to form a solid CdS cluster.



3.1.5 ZnO window

Basically, short wavelength light (<520 nm) is absorbed near the surface in the thick CdS layer and also does not generate any photocurrent. While a thin CdS layer allows no longer limited short wavelength collection in the CIGS layer. The transparent conducting materials can solve those problems. It has high resistivity and good transmission, leading to prevent current leakage (shunting) and especially can gain photocurrent by adjusting the band alignment. There are three main materials of the transparent conducting material class such as SnO_2 , $\text{In}_2\text{O}_3:\text{Sn}$ (ITO), and ZnO. SnO_2 requires high deposition temperatures that limit the potential of CIGS solar cell devices. It cannot withstand temperatures more than 200 to 250 °C after CBD-CdS process. For ITO and ZnO, it can both be used, but the most common material is ZnO which is favored by potentially lower material cost. Typically, the sputtering of doped ZnO films is preferred method for depositing the transparent window layer on CIGS device. ZnO has a wide band gap with an energy gap of 3.3 eV and also the large exciton energy of 60 meV at room temperature [9].

In this work, a ZnO layer is sputtered on the top of CdS layer. A radio frequency (RF) sputtering technique, where the substrates are rotated during deposition, is used to deposit an undoped ZnO layer (i-ZnO). Subsequently, the Al-doped ZnO or ZnO(Al) are deposited. The ZnO(Al) target has 2% weight of Al_2O_3 and 3N purity, while i-ZnO target has a purity of 4N. The RF powers are

80 W and 220 W for the i-ZnO and ZnO(Al) layers, respectively. The oxygen and argon gases are mutually flow during sputtering to form i-ZnO layer. But ZnO(Al) layer uses argon gas only. The highly resistive i-ZnO layer has a typical thickness of about 50 nm. The thickness of the ZnO(Al) is about 200 nm. In addition, ZnO(Al) has about 90% transparency and $10^{-4} \Omega\cdot\text{cm}$ of resistivity.

3.1.6 Al-grids

The CIGS solar cell device fabrication is finished by thermal evaporation of aluminum Al-grids above the window layer. The base pressure is about 8.0×10^{-6} mbar. This Al-grid is deposited onto the cells to facilitate the current collection and provide a contact electrode for current–voltage (J – V) measurement. The grids are evaporated from aluminum wire with 5N purity where the grid pattern is defined using a shadow mask. It is designed in order to allow as much light as possible in to the device. The aluminum also facilitates an ohmic contact with ZnO window layer and measuring probe as well. The grid thickness is about $1.8 \mu\text{m}$. The evaporation rate and film thickness are monitored with a quartz-crystal microbalance (QCM). Finally, after Al-grids evaporation, each cell area of 0.51 cm^2 is defined by mechanical scribing. 8 cells can be obtained on a $3 \text{ cm} \times 3 \text{ cm}$ substrate as shown in Fig.24.

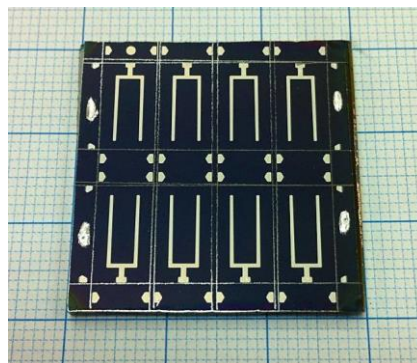


Figure 24 The complete CIGS solar cell device.

3.2 Wet-Etching Method

As mentioned in Chapter I, there are three wet chemical etchants to alter the CIGS surfaces in this study. One is acid such as aqua regia. The other is potassium hydroxide (KOH) and alcoholic potassium hydroxide (KOH+EtOH). The optimized concentrations and etching times were used in order to suitably control the etching rates. The thickness of CIGS films is fixed about 1.8 μm . The changes at the CIGS surfaces were studied in terms of roughness.

3.2.1 Aqua regia

Aqua regia is a mixture of hydrochloric (HCl) and nitric (HNO_3) acids. It consists of 3:1 concentration ratio of HCl: HNO_3 . Naturally, aqua regia is a yellow-orange fuming liquid. Upon mixing of concentrated HCl and HNO_3 acids, the chemical reaction occur in the volatile products of nitrosyl chloride and chlorine as evidenced fuming nature and characteristic yellow color of aqua regia. Aqua regia was first formulated and named by the European alchemist in the early 14th century. In that time, it is thought to be the universal etch for all metal and metallic compounds. It was the first solution for gold etching, and also the dissolving of platinum group (platinum, iridium, and osmium). The platinum group is slower etched than gold in aqua regia, even when using hot to boiling. In the industrial scale of gold refining, it can purified the highest quality (99.999%) gold. Moreover, aqua regia does etch a few other metal and compounds. It can be either a removal, polish, or preferential solution. On other metals, it acts as a surface cleaning solution only. Also, aqua regia is particularly useful for removal the contamination on surface of heavy metals such as copper, iron, etc. The aqua regia solution varies in constituent concentrations that may be diluted with water or alcohols. However, aqua regia quickly loses its effectiveness, it should usually only mixed immediately before use [15].

In this research, aqua regia conditions were done by varying the concentration ratio. Deionized water was used for diluting the solution to make the different aqua regia conditions. It is firstly to prepare 12 ml of hydrochloric acid (37%) in a beaker, then adding 4 ml of nitric acid (60%) slowly. Next,

mixing these acids together by magnetic stirring bar for 2 min, and also leave it cools down for about 1 min before use. All samples will be immersed into the solution beaker by using given etching times. After that, it will be rinsed and dried by deionized-water injection for about 30 s and nitrogen gas until it perfectly dries, respectively. The different aqua regia conditions are shown in Table 3.

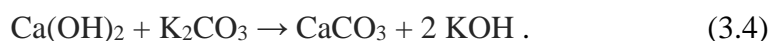
Table 3 The aqua regia etching conditions by varying etching times.

Condition	Initial substance	Concentration (Aqua regia : DI-water)	Etching times (s)
AR24_12	3HCl + HNO ₃	1 : 1	3
AR24_13	3HCl + HNO ₃	1 : 1	4
AR24_14	3HCl + HNO ₃	1 : 1	30
AR24_15	3HCl + HNO ₃	1 : 1	60

3.2.2 Potassium Hydroxide

Potassium hydroxide (KOH) is inorganic compound with a colorless solid. It is also called “caustic potash”. Potassium hydroxide is a prototypical strong base with translucent pellets. Lower molecular weight alcohols including methanol, ethanol, and propanol are excellent solvents. Naturally, potassium hydroxide is highly basic which strongly form alkaline solution in water and other polar solvents. Moreover, it is a useful alkali that has several applications with inorganic compounds depending upon solution concentration, and/or temperature. The concentration of 2-10 % mixture at room temperature is used for surface cleaning. For 30-40 % at room temperature to about 40 °C is good for general removal. And, more than 40% with boiling, it increasingly becomes preferential. Potassium hydroxide efficiently attacks oxide, such as silicon dioxide (SiO₂). Furthermore, it is highly preferential and used for dislocation in silicon and other single crystals [15]. Also, potassium hydroxide reacts with carbon dioxide (CO₂) to give bicarbonate (KHCO₃). In early 19th century, potassium hydroxide was prepared by adding the potassium carbonate (K₂CO₃)

to a strong solution of calcium hydroxide (Ca(OH)_2), leading to a metathesis reaction that caused calcium carbonate (CaCO_3) to precipitate, then leaving potassium hydroxide in solution. By filtering off the precipitated calcium carbonate and boiling down the solution, it gives potassium hydroxide. Following equation is a chemical reaction for the potassium hydroxide manufacturing [35].



Currently, it was largely replaced by the electrolysis of potassium chloride solution according to the below chemical reaction equation.



In this study, there are two potassium hydroxide solutions due to the solvents, such as deionized water and ethanol, by using an optimized concentration ratio in order to suitably control the etching rate. For the first potassium hydroxide solution, it was done by mixing 60 g of potassium hydroxide pellets (0.102 g per pellet) in 200 ml of deionized water. Upon the magnetic stirring bar and the occurrence chemical reaction, its temperature can ramped up to about 45°C. Almost about 10 min or until it is absolutely dissolved, a desired 30 % w/v (5.35 M) with pH 14 of potassium hydroxide solution would completely prepared and ready to use. Also, all samples are immersed into the solution beaker by using the given etching times, then, rinsed and dried by deionized water injection for about 30 s and nitrogen gas, respectively. The conditions of potassium hydroxide in this study are described in Table 4.

Table 4 The potassium hydroxide conditions by varying etching times.

Condition	Initial substance	Solvent	Concentration	pH	Etching times (s)
KOH2_1	60 g KOH pellets	200 ml DI-water	30 % w/v (5.35 M)	14	3
KOH2_2					4
KOH2_3					30
KOH2_4					60

3.2.3 Alcoholic Potassium Hydroxide

Alcoholic potassium hydroxide is prepared by using ethanol solvent in order to compare the etching results when using potassium hydroxide with deionized water. Alcoholic potassium hydroxide (KOH+EtOH) was used to etch CuInSe₂ film for monograin layer solar cell. The results show that it could remove preferentially Se, and the open-circuit voltage had decreased [18]. The other interesting motivation comes from an experiment on the texturisation of crystalline-silicon (c-Si) wafer. It was also studied by using alcoholic potassium hydroxide (KOH+Isopropanol) to produce the pyramidal shape of silicon film surface that can be seen in Fig.25 [36], [37].

For the preparation steps of alcoholic potassium hydroxide in this study, it is an analogous method to potassium hydroxide in deionized water. Similarly, it began by dissolving 60 g of potassium hydroxide pellets into 200 ml of ethanol, and, stirring them until it was perfectly dissolved. Etching step can be done by immersing the samples into the solution beaker by using given etching times. All conditions of alcoholic potassium hydroxide are summarized in Table 5.

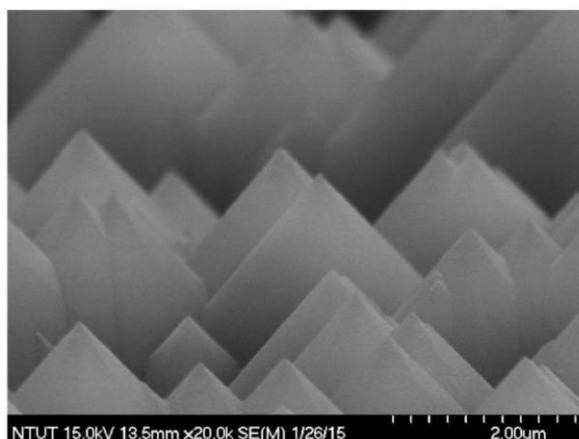


Figure 25 The SEM image of the surface of crystalline-silicon (c-Si) wafer after etching by dipping in a solution of H₂O/KOH/IPA (Isopropanol) [37].

Table 5 The alcoholic potassium hydroxide conditions by varying etching times.

Condition	Initial substance	Solvent	Concentration	pH	Etching times (s)
KOHE14_1	60 g KOH pellets	200 ml Ethanol	30 % w/v (5.35 M)	14	3
KOHE14_2					4
KOHE14_3					30
KOHE14_4					60

3.3 Characterization Techniques

3.3.1 Scanning Electron Microscopy (SEM)

In order to study film surface morphology, and micro- or nano-structure of matters, it needs to use a very special microscope. Scanning electron microscope (SEM) is a basic characterization tool for films and surfaces. The schematic SEM column is shown in Fig.26. The electron beam emits from a heated filament and are accelerated to an anode. There are two condenser lenses that focus the electron beam onto a very small spot size of diameter. By a pair of scanning coils that placed at the objective lens, the electron beam will be deflected to a specimen surface area. The electron beam has energy by accelerated voltage with a few kV to 30 kV. When the primary electrons hit and

transfer energy on the specimen. Electron and photon signals radiate from a teardrop-shaped interaction volume with various electronic excitations or energy spectrums. But there is an imaging mode based on electron signal used in this study, which is secondary electron mode. Secondary electron has the lowest energy portion of the emitted energy distribution. The signal is captured by a detector consisting of a scintillator/photomultiplier combination [38].

The JEOL JSM-7001F field emission scanning electron microscope (FESEM) was used to characterize the as-grown and modified CIGS surfaces in this study. It uses field emission gun which instead of the thermionic emitters in the traditional SEM. It does not heat the filament, the emission is reached by placing the filament in the huge electrical potential gradient. Especially, the FEG produces a cleaner image, less electrostatic distortion, and spatial resolution less than 2 nm. It also has the Schottky type field emission (T-FE) of electron source. The resolution can adjust up to 1.2 nm at 30 kV of electron accelerated voltage. There are two vacuum pumps in the FESEM. First is sputter-ion pumps in the electron beam system. The other is diffusion pump for sample chamber. In this study, the (30,000 \times) and (100,000 \times) magnifications were used in order to see more differences clearly.

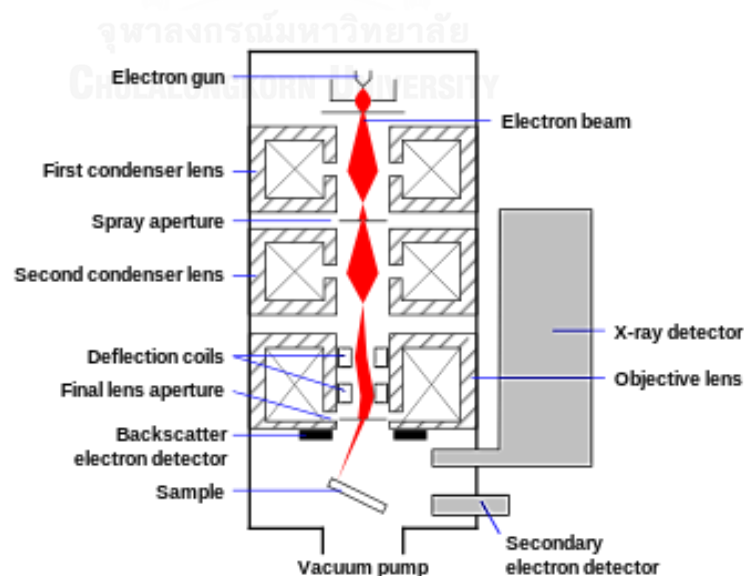


Figure 26 The typically schematic diagram of SEM column [39].

3.3.2 Atomic Force Microscopy (AFM)

The surface roughness of CIGS films can be analyzed by AFM technique. By interaction of atomic force between sample surface and probe, it results the simulated topography image. Basically, AFM contains a cantilever with very small and sharp tip (probe) at the end. Cantilever is an arched mechanical probe. Firstly, the laser beam is focused onto the tip of cantilever that it is moving on the sample surface. When tip is tow passing the sample surface, the atomic reaction forces between sample surface and tip can raise the cantilever to arch itself. This situation detects the magnitude of atomic forces at the distance between sample surface and tip atoms, leading to obtain a resulting energy which is interpreted signals then imaging the sample surface.

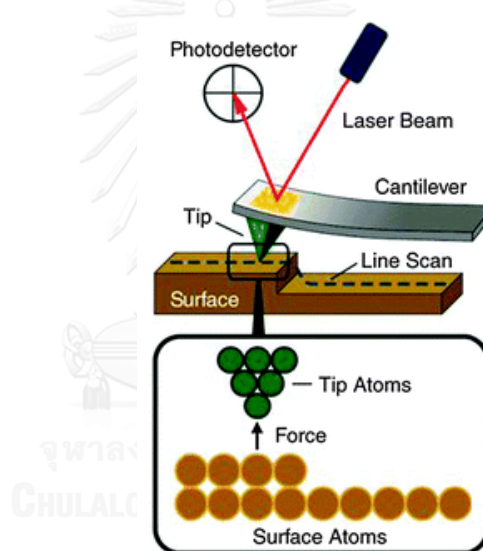


Figure 27 The principle of atomic force microscopy (AFM) [40].

The surface roughness value can be measured by a statistical analysis method. It represents the total roughness of sample surface which is calculated via the root mean square (rms) method. The distances between the highest and the lowest surface positions can be studied as z-range. The definition of surface roughness and z-range are shown by following equations,

$$\text{rms-roughness (Rq)} = \sqrt{\frac{\sum_{i=1}^N (h_i - \bar{h})^2}{N}}, \quad (3.6)$$

where h_i is an any height range, \bar{h} is an average height, and N_i is the number of averaged data;

$$z \text{ range} = h_{\max} - h_{\min} , \quad (3.7)$$

where h_{\max} is the maximum height of sample surface (nm) and h_{\min} is the minimum height of sample surface (nm).

The AFM (Veeco Dimension 3100) with tapping mode was used in the study. The tapping mode is an AFM imaging mode by keeping the probe closes enough to the sample for short-range forces to become detectable while preventing the tip from sticking with the sample surface. Tapping mode is frequently used AFM mode when operating in ambient conditions or in liquids. For the basic operating process, it is firstly to place sample on the specimen holder, then, adjust the sample to the laser beam position. Turn on a vacuum system for holding sample with the holder. Next, bring the tip down closing to the sample surface. It scans along the CIGS surfaces. The size of scanning images is $5 \mu\text{m} \times 5 \mu\text{m}$. The resolution of rms-roughness values is about 1 nm.

3.3.3 Current-Voltage (I-V) Measurement

The CIGS solar cell parameters being interested are short-circuit current (I_{sc}), open-circuit voltage (V_{oc}), fill factor (FF), and especially efficiency (η). The I-V measurement is a common method to determine those parameters. The I-V characteristic is the superposition of the I-V curve of solar cell diode in the dark with light-generated current. The light has the effect of shifting I-V curve which is down into the fourth quadrant where power can be extracted from the diode. Without illumination, a solar cell has the same characteristic as a diode. When light shines on the cell, the I-V curve shifts as the cell begins to generate power. So, with greater light intensity, the amount of shift will be greater.

In this research, the completed cell devices were measured by a Xenon lamp based solar simulator with a DC power supply and a voltage source/current measurement unit (Keithley model 237). The solar cell performance is

measured under the standard test condition (A.M. 1.5 at 25 °C). The intensity of light is always kept at 100 W/cm². The measurement unit is interfaced with a PC via IEEE-488 card. The data processing is controlled by Agilent VEE program.

3.3.4 External Quantum Efficiency (EQE) Measurement

Quantum efficiency is a tool to characterize the losses responsible for the difference in current. The light-generated current is the integral of the product of the external quantum efficiency (EQE) and also illumination spectrum. By illuminating, the information of photocurrent collection for each photon wavelength are revealed as an EQE curve. The quantum efficiency for solar cell is basically reduced due to the recombination effect. EQE is naturally due to the band gap of CIGS absorber layer, CdS buffer layer, ZnO window layer, and also a series of loss mechanisms. There are six main current loss mechanisms in the typical QE curve which are shown in Fig.28 and Table 6.

On the other hand, the internal quantum efficiency (IQE) refers to the efficiency with no reflected and transmitted photon out of the cell. By measuring the optical losses, the EQE curve can be corrected to obtain the IQE curve. Hence, QE result generally yields the properties of each layer comprising the cells. However, all CIGS solar cell devices in this study were interpreted via EQE only.

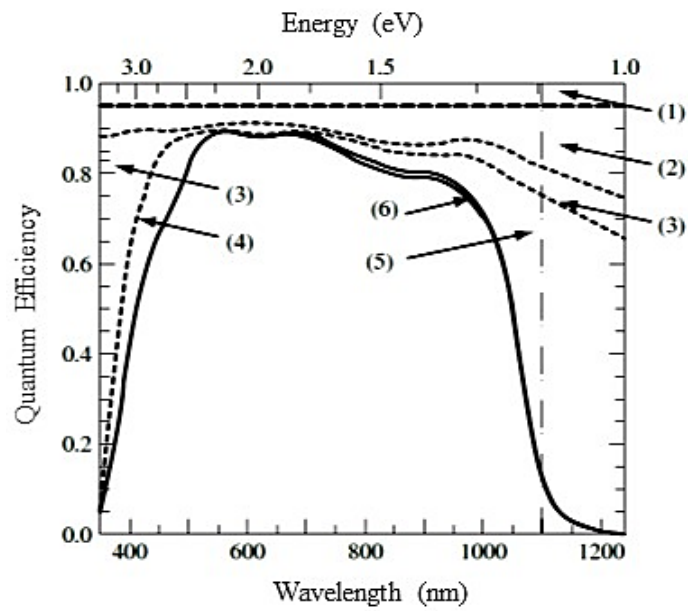


Figure 28 Quantum efficiency (solid lines) at 0 V and -1 V and optical losses for a Cu(In,Ga)Se₂/CdS solar cell in which the Cu(In,Ga)Se₂ has $E_g = 2.12$ eV [9].

Table 6 The optical and collection losses illustrated in Figure 28 for a typical Cu(In,Ga)Se₂/CdS solar cell [9].

Region in Fig.28	Optical loss mechanism	ΔJ (mA/cm ²)
(1)	Shading from grid with 4% area coverage	1.7
(2)	Reflection from Cu(In,Ga)Se ₂ /CdS/ZnO	3.8
(3)	Absorption in ZnO	1.8
(4)	Absorption CdS	0.8
(5)	Incomplete generation in Cu(In,Ga)Se ₂	1.9
(6)	Incomplete generation in Cu(In,Ga)Se ₂	0.4

CHAPTER IV

RESULTS AND DISCUSSION

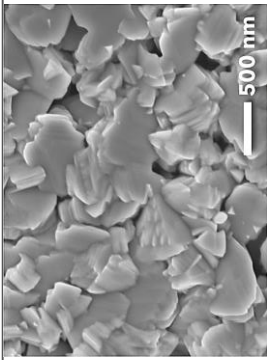
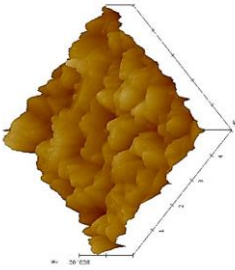
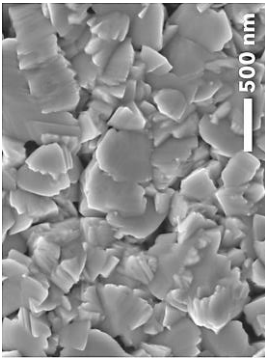
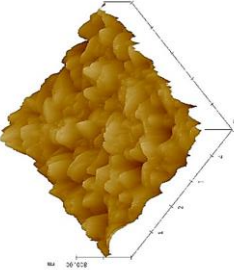
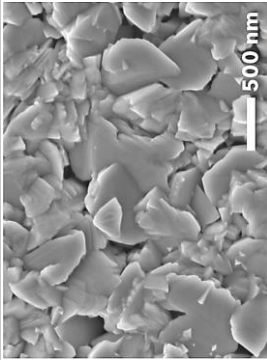
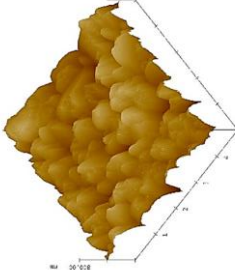
In this chapter, I will discuss and compare the results of the non-etched CIGS surface with the altered CIGS surface in order to study the relationship between the roughness of CIGS surface and the efficiencies of the CIGS solar cells. There are three chemical solutions that I made some attempts, e.g. aqua regia, potassium hydroxide (KOH), and alcoholic potassium hydroxide (KOH+EtOH). I found that aqua regia could significantly affect the CIGS surface roughness and especially solar cell parameters. Moreover, the spectral response results will also be discussed.

4.1 Surface morphology and RMS roughness

The FESEM images of potassium hydroxide and alcoholic potassium hydroxide etching conditions are shown in Table 7 and 8, respectively. Both of them tend to result in unchanged surfaces when compared with the non-etched surface. However, the AFM analysis could clearly reveal that their etched CIGS surfaces changed a little bit. Even at longer etching times (more than 60 s), the roughness did not change. The rms roughness values of those conditions are also described in last column of Table 7 and 8.

On the other hand, the FESEM results of aqua regia conditions at 3, 4, 30, and 60 s etching times are shown in Table 9. At 3 and 4 s of etching times, it could not visually change the CIGS surface when compared with the non-etched surface condition. While etching at 30 and 60 s the changes could be clearly seen. It shows very small size of pores distributing around the CIGS surface. Etching at 60 s results in higher number of pores than etching at 30 s. The existence of these pores is believed to create rougher surface, but the rms roughness indicates that etching with 4 s produced very rough surface than the others. Hence, it is proved that etching at 30 s and 60 s could make smoother surface with pores.

Table 7 The FESEM and AFM results of potassium hydroxide (KOH) etching conditions.

Condition	Chemical etchant	Etching time (s)	FESEM image	AFM image (5 × 5 μm)	rms roughness (nm)
Non-etch	-	-			59
KOH2_1	Potassium hydroxide (KOH)	3			59
KOH2_2	Potassium hydroxide (KOH)	4			60

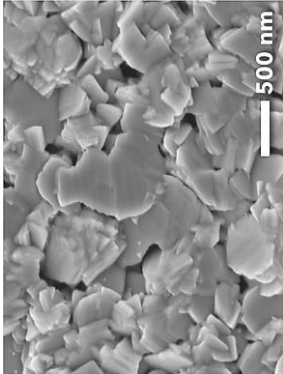
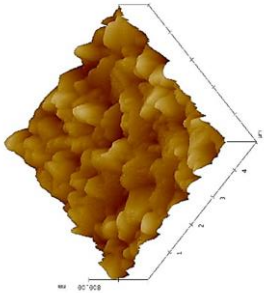
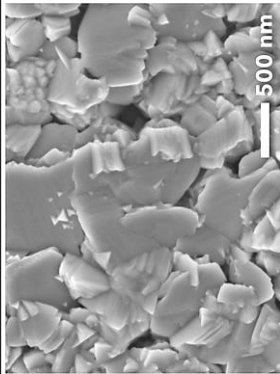
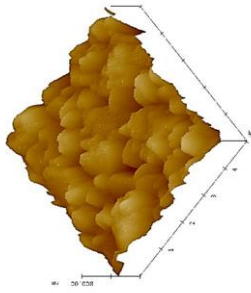
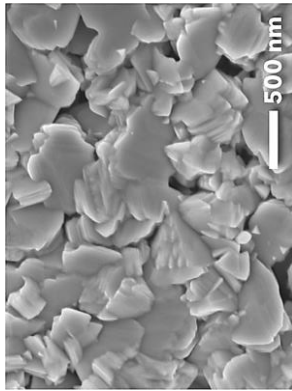
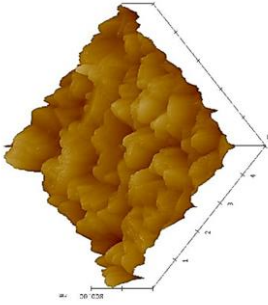
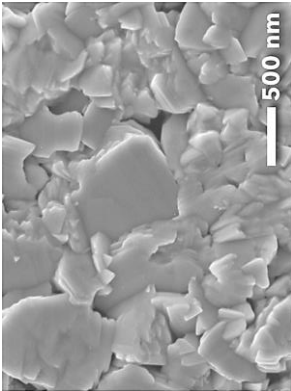
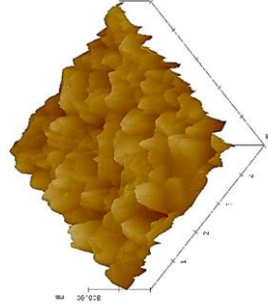
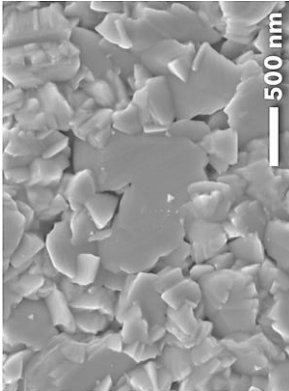
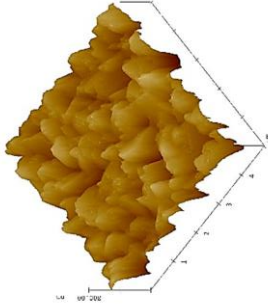
Condition	Chemical etchant	Etching time (s)	FESEM image	AFM image (5 × 5 μm)	rms roughness (nm)
KOH2_3	Potassium hydroxide (KOH)	30			59
KOH2_4	Potassium hydroxide (KOH)	60			59

Table 8 The FESEM and AFM results of alcoholic potassium hydroxide (KOH+EtOH) etching conditions.

Condition	Chemical etchant	Etching time (s)	FESEM image	AFM image (5 × 5 μm)	rms roughness (nm)
Non-etch	-	-			59
KOHE14_1	Alcoholic potassium hydroxide (KOH+EtOH)	3			60
KOH14_2	Alcoholic potassium hydroxide (KOH+EtOH)	4			59

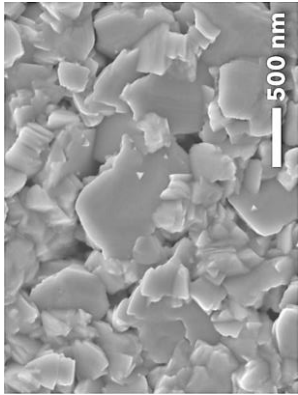
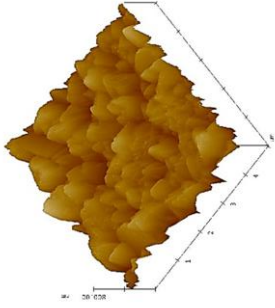
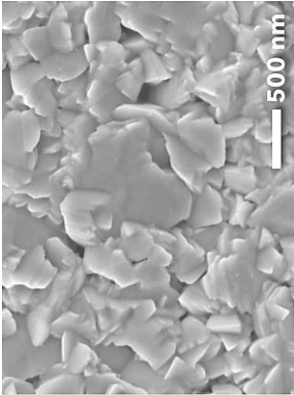
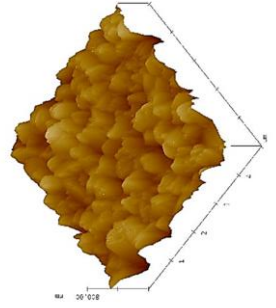
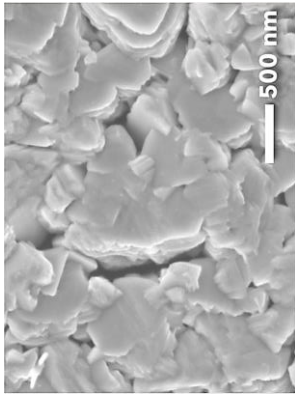
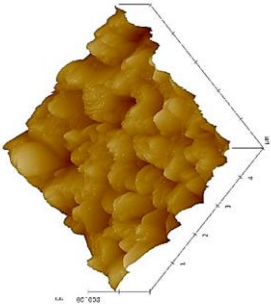
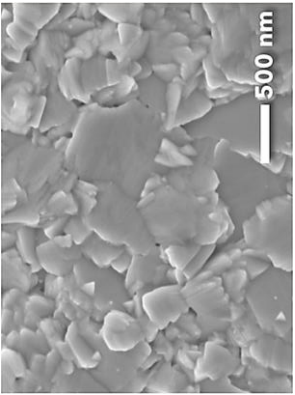
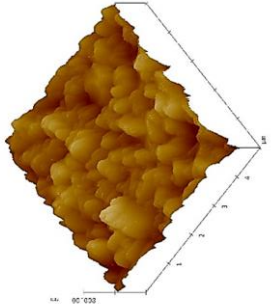
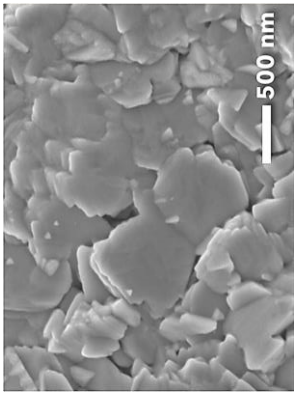
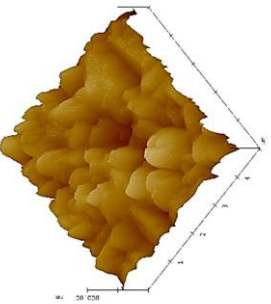
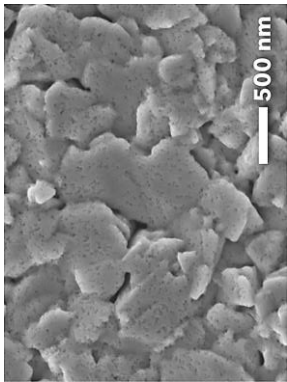
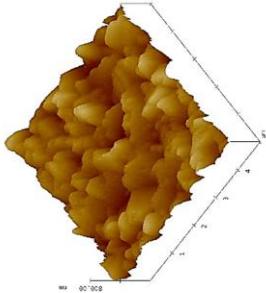
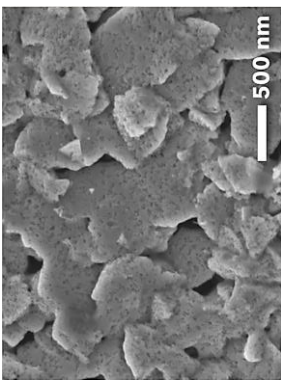
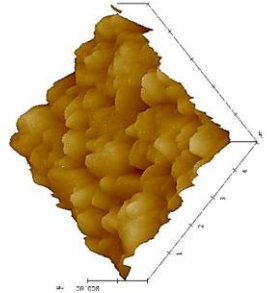
Condition	Chemical etchant	Etching time (s)	FESEM image	AFM image (5 × 5 μm)	rms roughness (nm)
KOHE14_3	Alcoholic potassium hydroxide (KOH+EtOH)	30			59
KOHE14_4	Alcoholic potassium hydroxide (KOH+EtOH)	60			59

Table 9 The FESEM and AFM results of aqua regia etching conditions.

Condition	Chemical etchant	Etching time (s)	FESEM image	AFM image (5 × 5 μm)	rms roughness (nm)
Non-etch	-	-			59
AR24_12	Aqua regia (1:1)	3			62
AR24_13	Aqua regia (1:1)	4			71

Condition	Chemical etchant	Etching time (s)	FESEM image	AFM image (5 × 5 μm)	rms roughness (nm)
AR24_14	Aqua regia (1:1)	30			56
AR24_15	Aqua regia (1:1)	60			57

The surface morphology and rms roughness results are summarized in Table 10. The aqua regia etching conditions significantly changed CIGS surface roughness. It shows that there is extremely etched CIGS surface at 3 s to 4 s and the rms roughness immediately increases up to 71 nm. At longer etching times, the rms roughness decreases down to 56 nm, while at 30 s to 60 s the roughness remains constant. In contrast, potassium hydroxide and alcoholic potassium hydroxide etchings barely affect the CIGS surface roughness. Their rms roughness values are almost the same even at longer etching times. Nevertheless, etching with aqua regia more than a minute decreases the thickness of CIGS film, and leaves more chemical residues.

Table 10 The comparison of surface morphology and rms roughness results of aqua regia, KOH, and KOH+EtOH etching conditions.

Condition	Chemical etchant	Conc.	Etching time (s)	rms roughness (nm)	Note
Non-etch	-	-	-	59	-
AR24_12	Aqua regia	1 : 1	3	62	Rougher
AR24_13	Aqua regia	1 : 1	4	71	Rougher
AR24_14	Aqua regia	1 : 1	30	56	Smoother + Pore
AR24_15	Aqua regia	1 : 1	60	57	Smoother + Pore
KOH2_1	KOH	30 % w/v	3	59	Unchanged
KOH2_2	KOH	30 % w/v	4	60	Unchanged
KOH2_3	KOH	30 % w/v	30	59	Unchanged
KOH2_4	KOH	30 % w/v	60	59	Unchanged
KOHE14_1	KOH+EtOH	30 % w/v	3	60	Unchanged
KOHE14_2	KOH+EtOH	30 % w/v	4	59	Unchanged
KOHE14_3	KOH+EtOH	30 % w/v	30	59	Unchanged
KOHE14_4	KOH+EtOH	30 % w/v	60	59	Unchanged

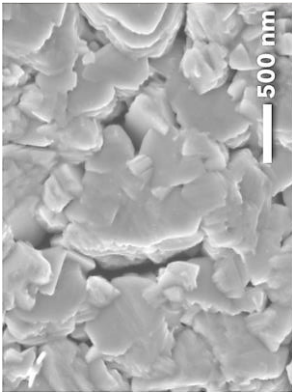
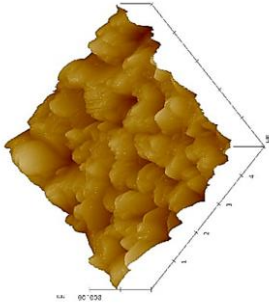
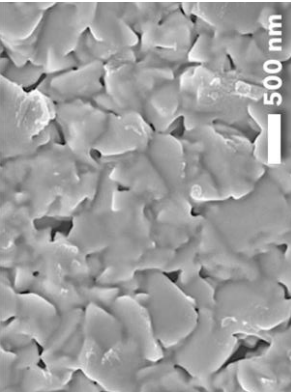
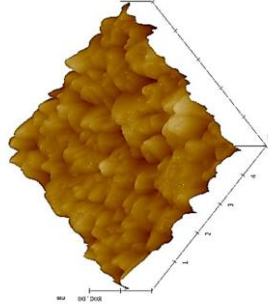
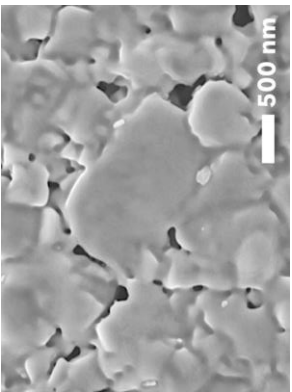
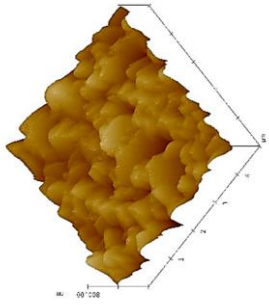
Accordingly, to make different CIGS surface roughness such as rougher or smoother surfaces. Aqua regia concentration was varied and etching times are shown in Table 11. Also, the FESEM and AFM results of these different aqua regia conditions are displayed in Table 12.

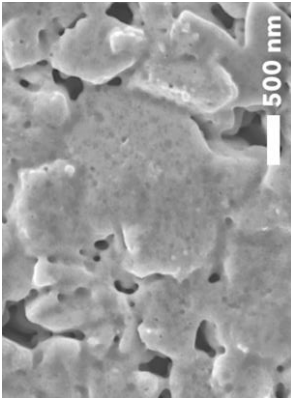
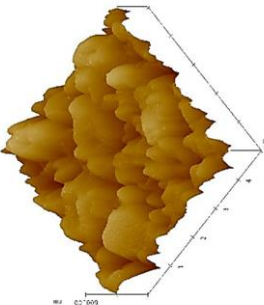
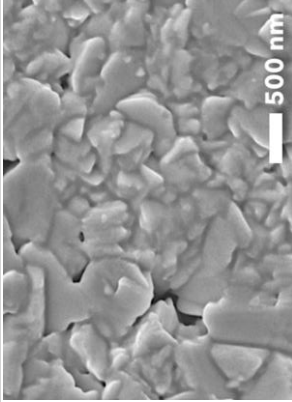
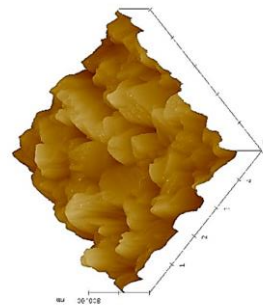
Table 11 The different aqua regia etching conditions by varying concentrations and etching times.

Condition	Initial substance	Concentration (Aqua regia : DI-water)	Etching times (s)
AR20_16	3HCl + HNO ₃	1 : 0	3
AR20_17	3HCl + HNO ₃	1 : 0	4
AR21_6	3HCl + HNO ₃	2 : 1	30
AR22_2	3HCl + HNO ₃	3 : 2	3

In Table 12, using aqua regia without mixing with deionized water (pure aqua regia) at a few seconds shows smoother CIGS surfaces at increasing etching time. Etching conditions of AR20_16 and AR20_17 show smoother surfaces, while AR21_6 shows rougher surface with pores and has higher rms roughness than the non-etch condition. Moreover, AR22_2 condition created very rough CIGS surfaces, and thickness is deteriorated when etching at longer times. The aggregation of grains in AR22_2 causes very rough CIGS surface. Although, AR21_6 approximately gives the same rms roughness value with AR24_13 that is about 71 nm, it is rougher surface with pored while AR24_13 has no pored at all. The thickness of altered CIGS films via aqua regia etchings is changed about a few nanometers by surface roughness modification.

Table 12 The FESEM and AFM results of different aqua regia conditions by varying concentrations and etching times.

Condition	Concentration ratio (Aqua regia : DI- water)	Etching time (s)	FESEM image	AFM image (5 × 5 μm)	rms roughness (nm)
Non-etch	-	-			59
AR20_16	1:0	3			53
AR20_17	1:0	4			57

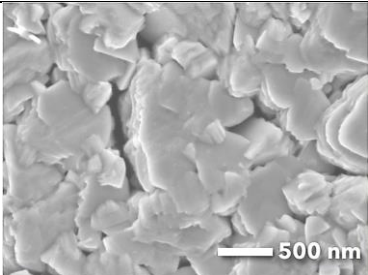
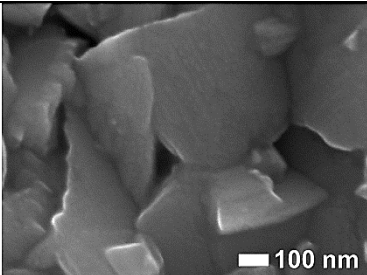
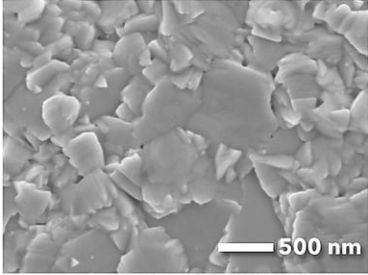
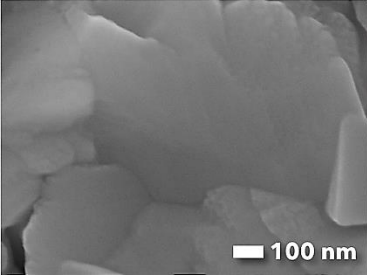
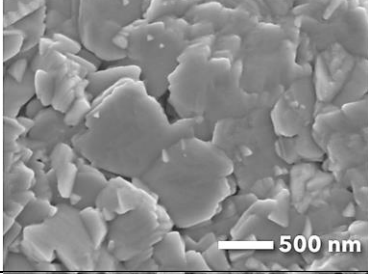
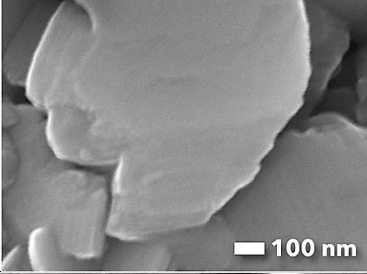
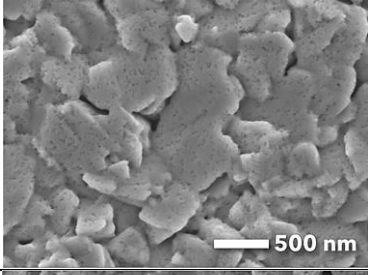
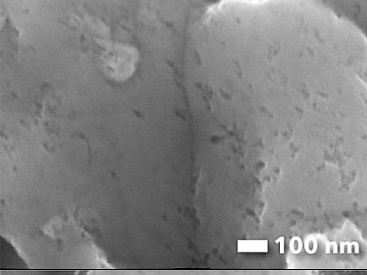
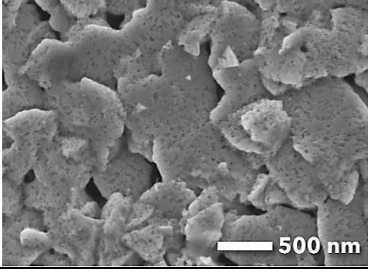
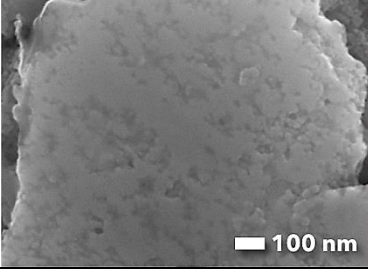
Condition	Concentration ratio (Aqua regia : DI- water)	Etching time (s)	FESEM image	AFM image (5 × 5 μm)	rms roughness (nm)
AR21_6	2:1	30			71
AR22_2	3:2	3			84

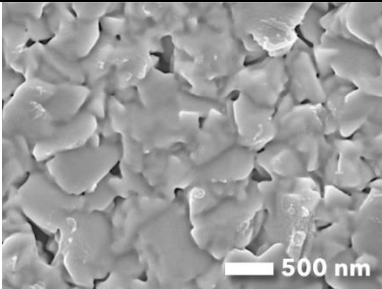
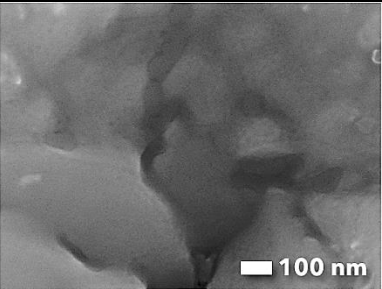
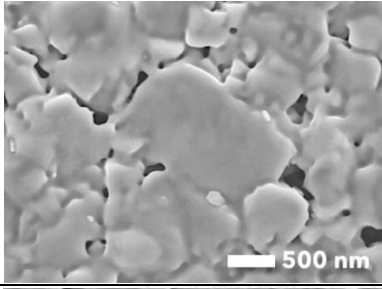
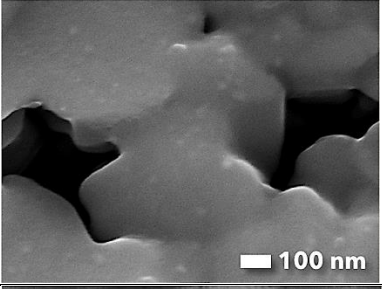
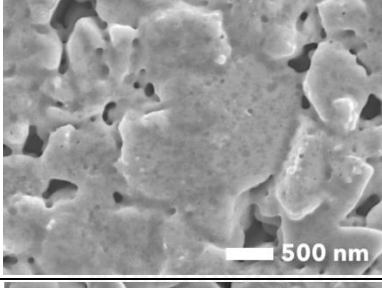
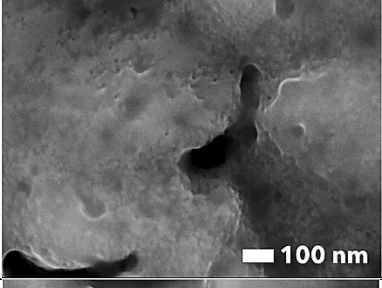
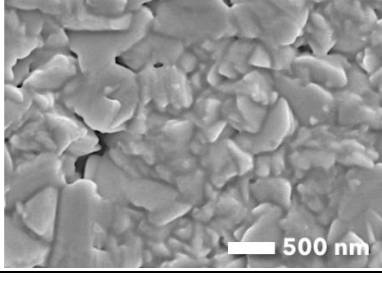
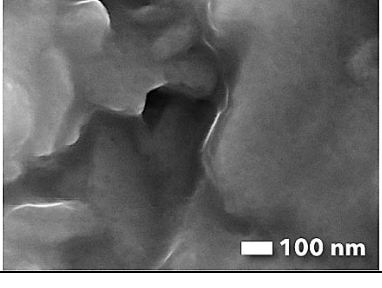
In order to visually observe more differences an etched CIGS surfaces in each aqua regia etching conditions, it needs to zoom in or use higher magnification (100,000×), that can reveal more details. The results between high and low magnifications FESEM images of different aqua regia etching conditions can be seen in Table 13.

The AR24_13 condition clearly shows the aggregation of grains that produces high rms roughness up to about 71 nm. The edges of the grain become noticeably sharper. Also, very small pores or holes in both AR24_14 and AR24_15 conditions can be observed. The number of pores depend on etching times which AR24_15 has higher number of pores than AR24_14. The size of pores in AR24_14 condition is approximately less than 100 nm, while AR24_15 condition show larger size than 100 nm. However, the occurrence of larger pores can be seen as a scratch, some of them are likely a hole-line that distribute around the main area of grains and boundaries. The grain boundaries in AR20_16 and AR20_17 conditions evidently merge together that create smoother surfaces. The AR21_6 condition shows rough surface with various pore sizes which produce higher rms roughness value. The shape and size of pores in AR24_14 and AR24_15 clearly differ from AR21_6. In addition, the AR22_2 condition shows the aggregation of grains on the rims that cause very rough surface.

CHULALONGKORN UNIVERSITY

Table 13 The FESEM images of different aqua regia etching conditions with 30,000× and 100,000× magnification.

Condition	FESEM image	
	30,000×	100,000×
Non-etch		
AR24_12 (1:1, 3 s)		
AR24_13 (1:1, 4 s)		
AR24_14 (1:1, 30 s)		
AR24_15 (1:1, 60 s)		

Condition	FESEM image	
	30,000×	100,000×
AR20_16 (1:0, 3 s)		
AR20_17 (1:0, 4 s)		
AR21_6 (2:1, 30 s)		
AR22_2 (3:2, 3 s)		

4.2 J-V curves

The effect of the modified CIGS surfaces on solar cell parameters can be studied by J-V characteristics. It showed that potassium hydroxide (KOH) and alcoholic potassium hydroxide (KOH+EtOH) etching conditions correspondingly produced lower solar cell parameters than the non-etched condition such as short-circuit current density (J_{sc}) and also open-circuit voltage (V_{oc}) which can be seen in Fig.29 and 30. Also, the rms roughness and solar cell parameters of both hydroxide conditions can be shown in Table 14. Potassium hydroxide tends to decrease the values of solar cell parameters. Alcoholic potassium hydroxide closely shows the same solar cell parameters as the non-etched condition especially an efficiency when etching at 30 s. It indicated that alcoholic potassium hydroxide did not affect the solar cell parameters. However, series resistance (R_s) and shunt resistance (R_{sh}) in both hydroxide conditions are clearly higher and lower than the non-etched condition, respectively.

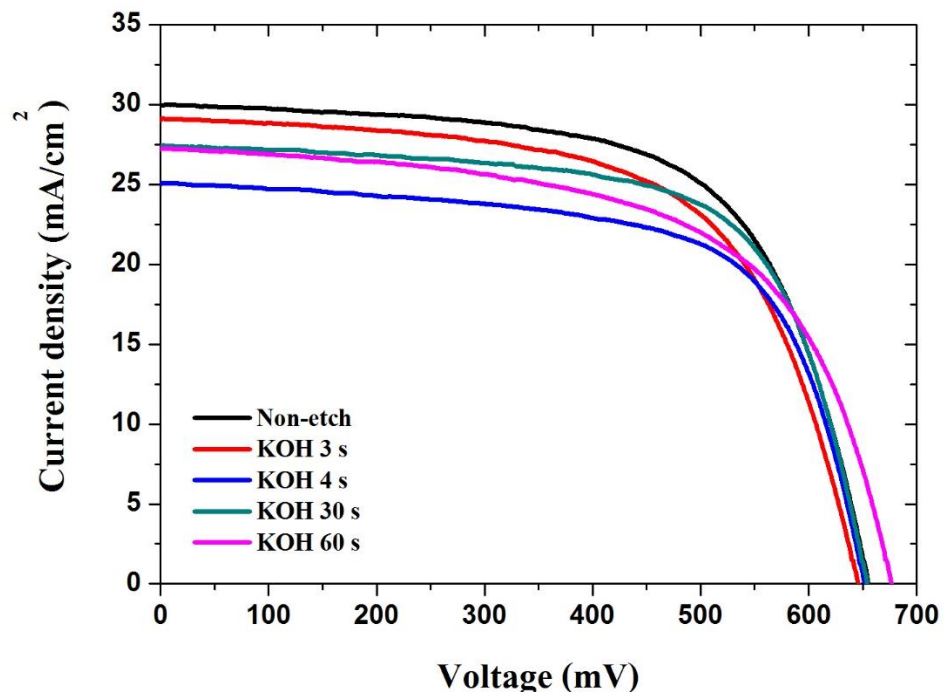


Figure 29 The J-V curves of potassium hydroxide etching conditions.

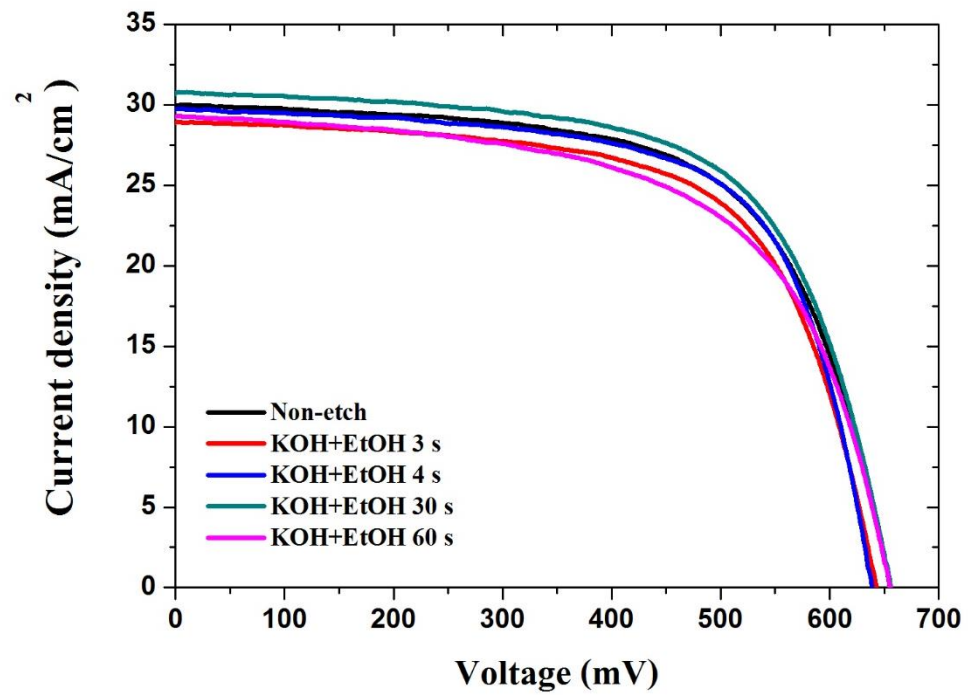


Figure 30 The J-V curves of alcoholic potassium hydroxide etching conditions.

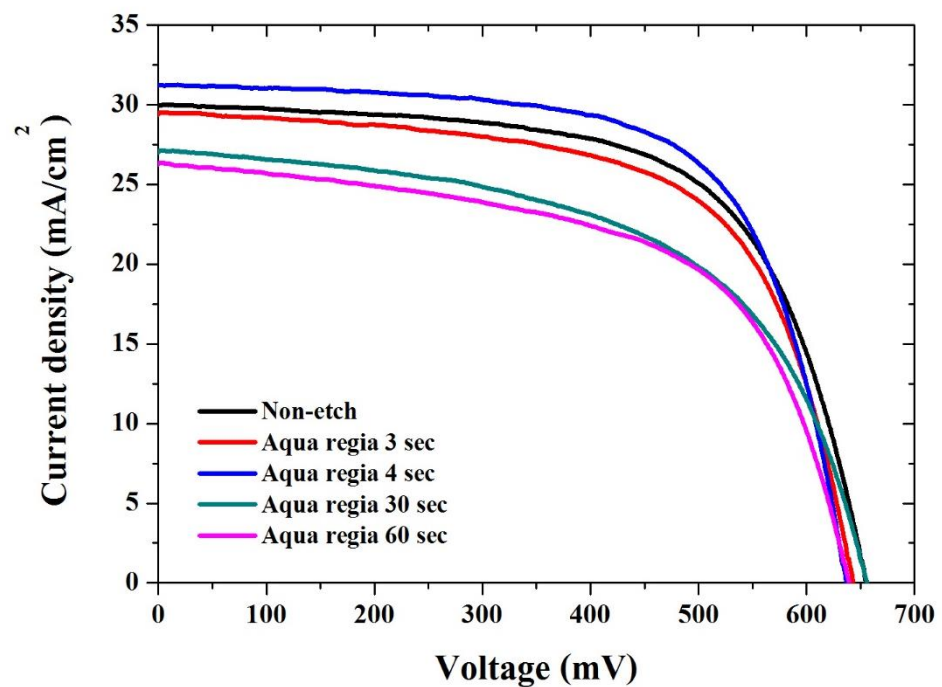


Figure 31 The J-V curves of aqua regia etching conditions.

Table 14 The rms roughness values and solar cell parameters of potassium hydroxide and alcoholic potassium hydroxide etching conditions.

Condition	Chemical etchant	Etching times (s)	rms roughness (nm)	J_{sc} (mA/cm ²)	V_{oc} (mV)	η (%)	FF (%)	R_s (Ω /cm ²)	R_{sh} (Ω /cm ²)
Non-etch	-	-	59	29.9	636	13.1	67.6	0.5	2178
KOH2_1	KOH	3	59	29.0	646	11.6	61.8	1.8	882
KOH2_2	KOH	4	60	25.2	658	11.6	61.4	2.2	631
KOH2_3	KOH	30	59	27.3	654	11.9	66.9	1.4	837
KOH2_4	KOH	60	59	27.0	677	11.0	59.9	1.2	690
KOHE14_1	KOH+EtOH	3	60	29.3	653	11.8	61.5	1.0	844
KOHE14_2	KOH+EtOH	4	59	29.9	639	12.6	66.1	0.9	1209
KOHE14_3	KOH+EtOH	30	60	30.7	656	13.0	64.4	1.1	1200
KOHE14_4	KOH+EtOH	60	60	29.2	655	11.5	60.1	1.1	945
AR24_12	Aqua regia	3	62	29.8	643	12.5	62.7	0.8	1854
AR24_13	Aqua regia	4	71	31.9	637	13.4	67.7	1.2	2535
AR24_14	Aqua regia	30	56	26.8	649	9.7	55.9	1.3	330
AR24_15	Aqua regia	60	57	26.3	639	9.8	58.7	1.3	390

On the other hand, an aqua regia etching condition could achieve higher J_{sc} , as shown in Fig.31. It is a condition with 1:1 ratio at 4 sec or AR24_13 (blue line) that significantly produced higher J_{sc} and V_{oc} than the other conditions especially the non-etched condition (black line). Moreover, it produced high efficiency, fill factor and shunt resistance as well. Normally, the reduction of J-V curves causes by decreased shunt resistance (R_{sh}) and increased series resistance (R_s), leading to lower fill factors. This means that the quality of p-n junction and carrier path throughout might be enhanced.

Hence, the different aqua regia etching conditions in Table 14 were also studied in term of J-V curves and solar cell parameters. The trend of J-V curves of different aqua regia etching conditions can be seen in Fig.32, and the solar cell parameters are shown in Table 15.

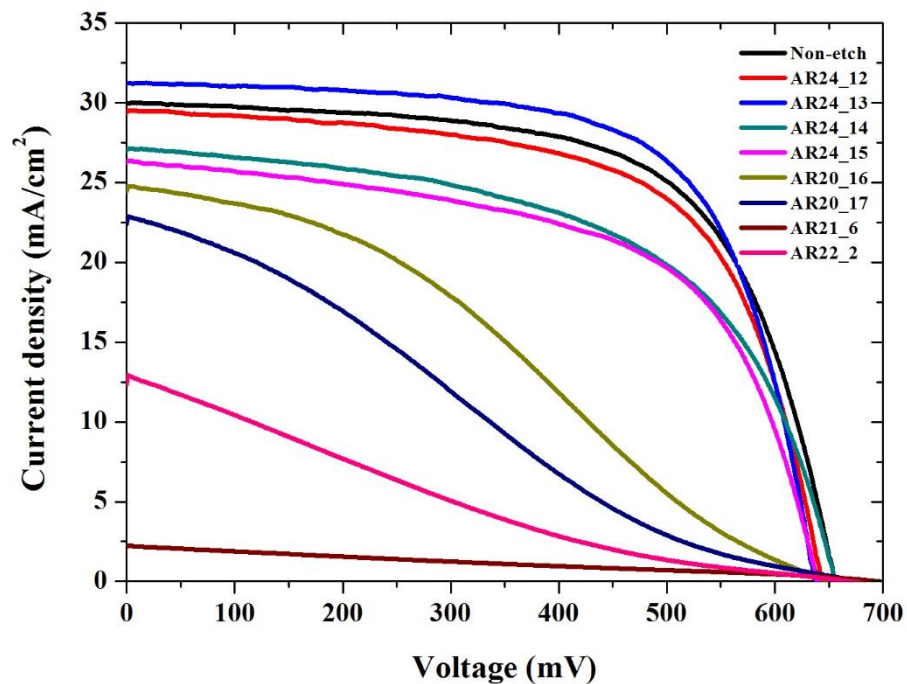


Figure 32 The J-V curves of different aqua regia etching conditions.

Table 15 The rms roughness values and solar cell parameters of different aqua regia etching conditions.

Condition	Concentration ratio	Etching times (s)	rms roughness (nm)	J_{sc} (mA/cm ²)	V_{oc} (mV)	η (%)	FF (%)	R_s (Ω /cm ²)	R_{sh} (Ω /cm ²)
Non-etch	-	-	59	29.9	636	13.1	67.6	0.5	2178
AR24_12	1 : 1	3	62	29.8	643	12.5	62.7	0.8	1854
AR24_13	1 : 1	4	71	31.9	637	13.4	67.7	1.2	2535
AR24_14	1 : 1	30	56	26.8	649	9.7	55.9	1.3	330
AR24_15	1 : 1	60	57	26.3	639	9.8	58.7	1.3	390
AR20_16	1 : 0	3	53	22.4	678	3.7	22.4	12.4	223
AR20_27	1 : 0	4	51	24.4	651	5.4	33.9	10.0	487
AR21_6	2 : 1	30	71	2.4	696	0.4	23.5	21.1	223
AR22_2	3 : 2	3	84	12.3	670	1.6	19.3	15.0	88

In Fig.32, most of aqua regia etching conditions except AR24_12 and AR24_13 tend to worsen the situation. The trend of J_{sc} subsequently dropped with the conditions of pure aqua regia (AR20_16 and AR20_17), AR21_6, and AR22_2, whereas V_{oc} tends to increase. In Table 15, it shows that AR24_13 achieved the highest efficiency of about 13.4%. Moreover, J_{sc} and R_{sh} significantly increase. The conditions of AR21_6 and AR24_13 show similar results of the same rms values, but their solar cell parameters are extremely different with AR21_6 having the lowest efficiency. Very rough CIGS surface of AR22_2 condition gave the lowest current density.

Briefly, the relationship between rms roughness values and solar cell parameters in Table 15 can be plotted in Fig.33, 34, 35, and 36 with the dash line representing the rms roughness value of non-etched condition. Smoother CIGS surfaces and also very rough CIGS surfaces (AR22_2) tend to produce lower J_{sc} , fill factor and also efficiencies, but higher V_{oc} . Noticeably, the conditions of AR21_6 and AR24_13 similarly show the same rms roughness values. But their surface characteristics are clearly different. The AR21_6 condition produced rougher and pored CIGS surface roughness, leading to highest V_{oc} , but lowest J_{sc} , FF, and especially efficiency. Whilst, the AR24_13 condition resulted rougher CIGS surface without pores distributing around the grain boundaries as shown in FESEM images results. Also, AR24_13 condition gave unique results in terms of surface morphology, rms roughness, and solar cell parameters as well. At this point, it indicates that the CIGS surface feature is necessary to consider for manufacturing CIGS solar cell devices, because even it has the same rms roughness values, perhaps they have different surface features. Also, it directly affects the formation of p-n junction or electronic structure. Rougher surfaces without pored have higher probability to collect the incident light, thus generating more photocurrent or light trapping, and leading to better solar cell performance. Smooth surface features produce higher light scattering instead. As a result, rougher CIGS surface with sharper grain boundary (AR24_13) significantly results in higher solar cell parameters, it may be an optimal surface feature.

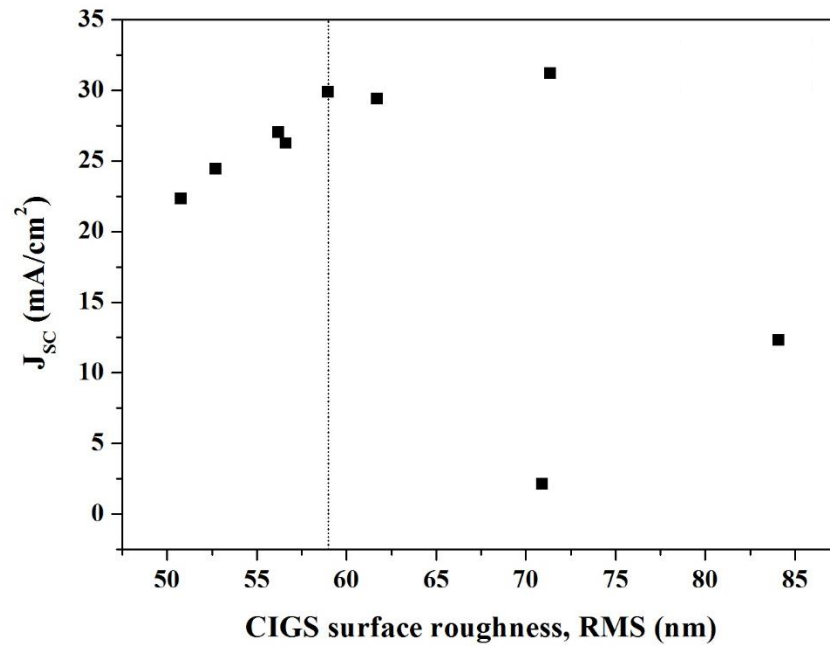


Figure 33 The trends of short-circuit current density (J_{sc}) vs. rms roughness of different aqua regia etching conditions.

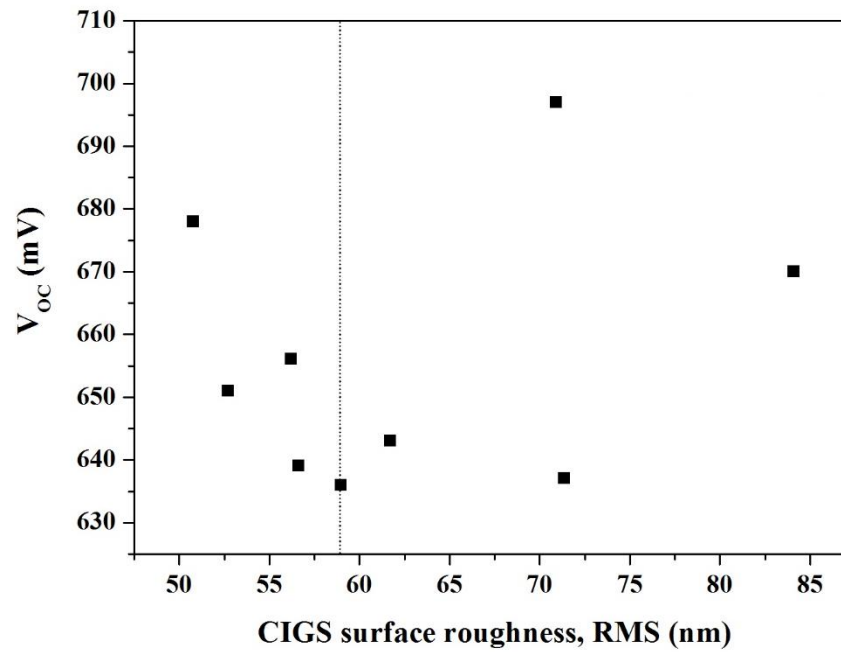


Figure 34 The trends of open-circuit voltage (V_{oc}) vs. rms roughness of different aqua regia etching conditions.

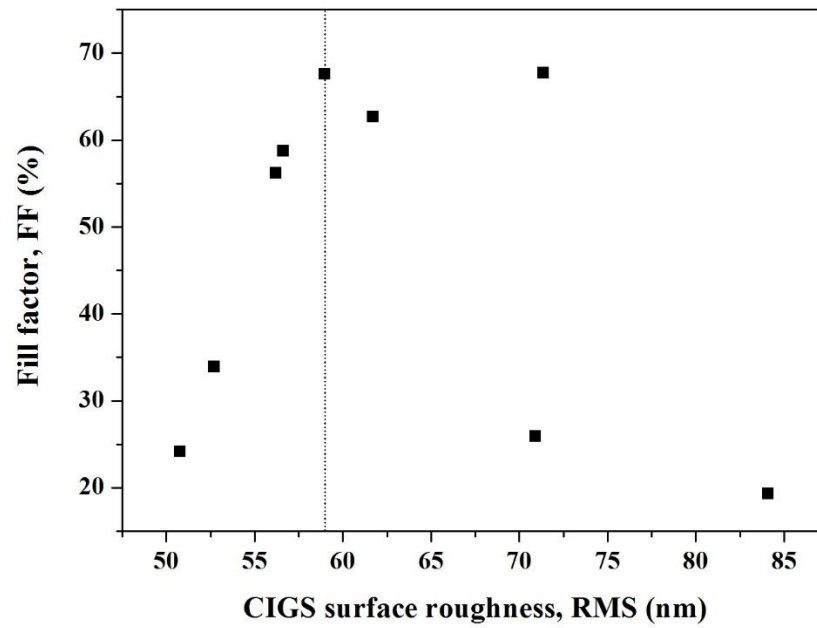


Figure 35 The trends of fill factor (FF) vs. rms roughness of different aqua regia etching conditions.

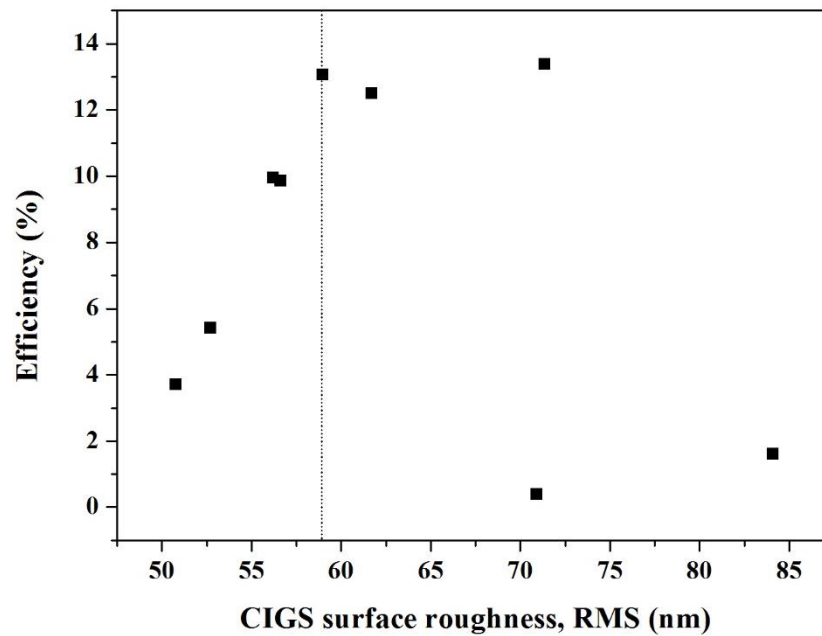


Figure 36 The trends of efficiency (η) vs. rms roughness of different aqua regia etching conditions.

4.3 Spectral responses

The EQE curves of altered CIGS surfaces relatively correspond to the J-V curves. Etching with potassium hydroxide evidently resulted in lower EQE curves than the non-etched condition even etching at very short times as shown in Fig.37. For alcoholic potassium hydroxide etching condition, it is closed to the non-etched condition, which can be seen in Fig.38. At short wavelength (350–500 nm), it represents the light absorption ranges for the energy gaps of ZnO-window layer and CdS-buffer layer, respectively. Here, the EQE curves of both hydroxide conditions are similar to the non-etched condition at short wavelength, i.e. it really did not affect thin film layers above the CIGS. Since wavelength above 600 nm, it is a range of light absorption in CIGS, it suggests that the lower EQE curves come from low carrier collection in CIGS bulk thus generating lower photocurrent.

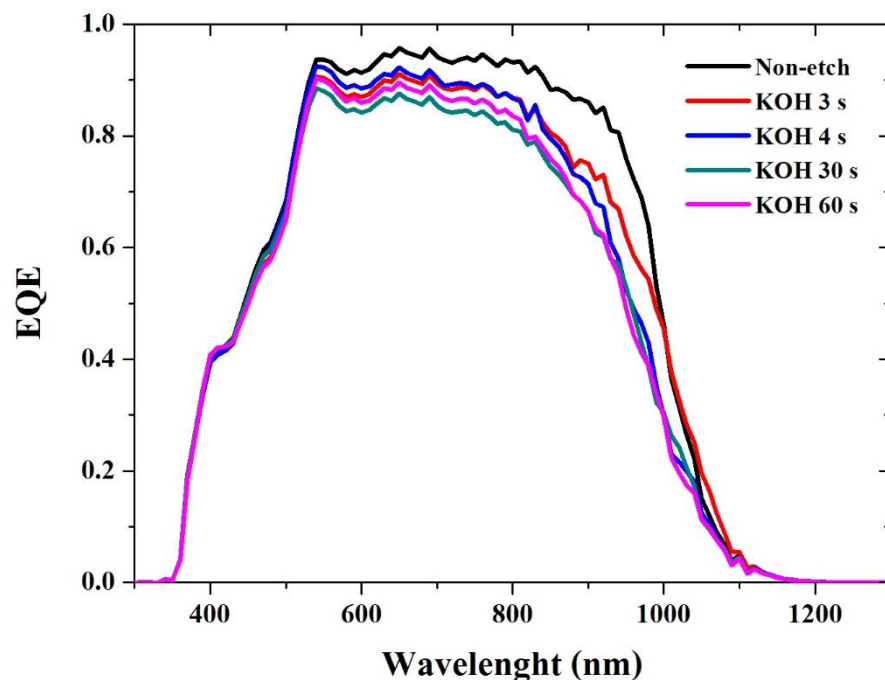


Figure 37 The EQE curves of potassium hydroxide (KOH) etching conditions.

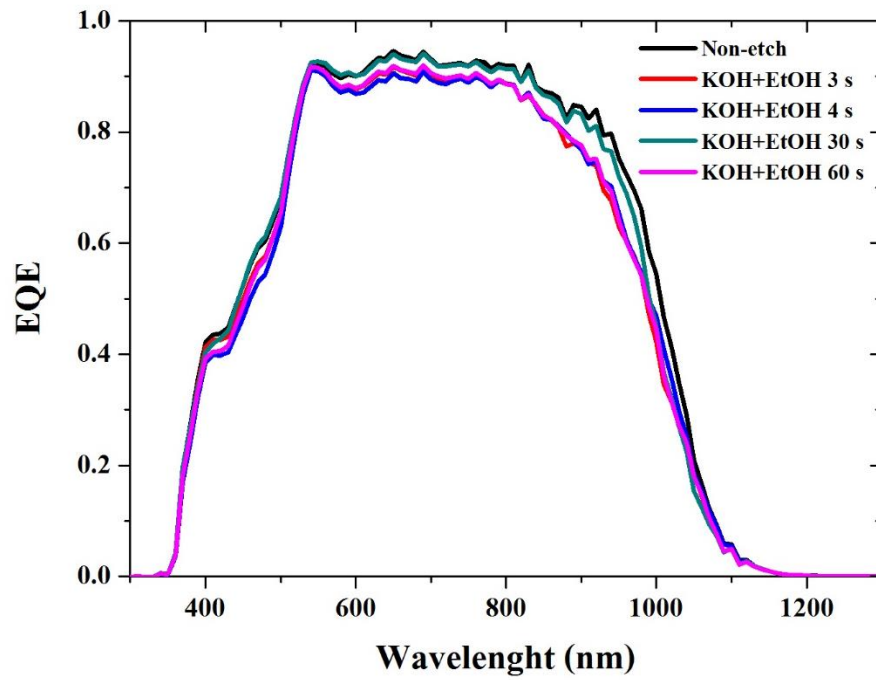


Figure 38 The EQE curves of alcoholic potassium hydroxide (KOH+EtOH) etching conditions.

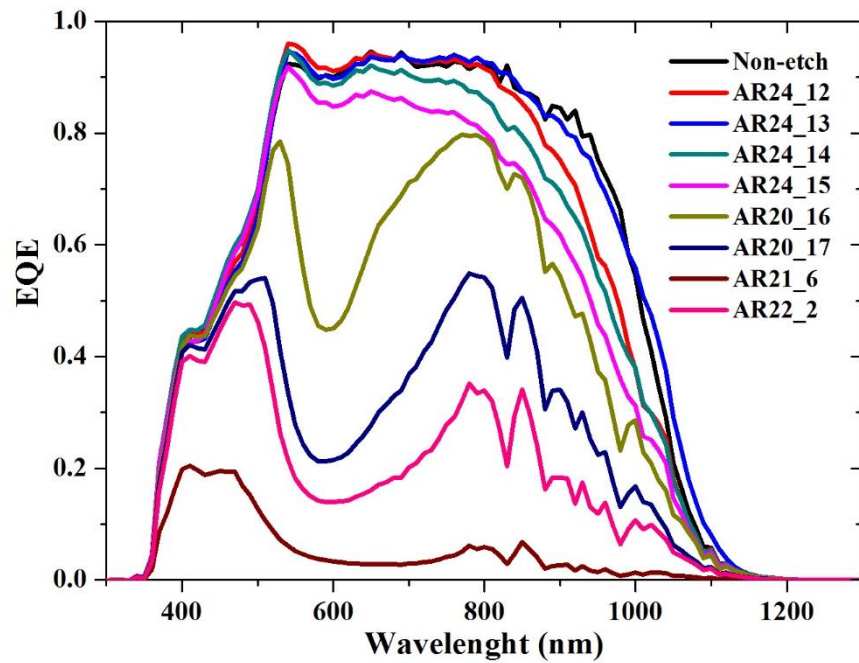


Figure 39 The EQE curves of different aqua regia etching conditions.

Besides, the possible explanation is that both hydroxide etching conditions will not affect the CIGS surface roughness. Potassium hydroxide never helps to improve CIGS solar cell performance, actually worsen the situations. It possibly comes from the changes of chemical compositions at etched CIGS surfaces. Some chemical reaction mechanisms occur during etching processes, leading to subsequent lower J-V and EQE curves.

For the EQE curves of etched CIGS surfaces by various aqua regia etching conditions in Fig.39. The conditions of AR24_12, AR24_13, and AR24_14 show slightly higher EQE curves at about 550 nm. It indicates that the CdS/CIGS interface might be improved, leading to reduction of interface recombination and generate more photocurrent. The reduction of EQE curves at long wavelength is caused by incomplete collection effects. Some charge carriers deep inside CIGS absorber are probably recombined before reaching the space charge region (SCR). Lower EQE curves at short wavelength are due to the large number of carriers which generated by optical absorption in ZnO and CdS layers are recombined and cannot contribute to collected photocurrent. The main optical losses in other aqua regia etching conditions come from recombination at CdS/CIGS interface and incomplete collection in CIGS bulk. Hence, it is confirmed that very rough, and even smoother with pored CIGS surfaces result in lower EQE curve at short wavelength, leading to low photocurrent at CdS/CIGS interface or increasing chances of recombinations. As mentioned, this situation directly affects to the carrier collection in CIGS bulk. On the other hand, the latter four aqua regia etching conditions refer to the destruction at the CIGS surfaces. The long wavelength at about 800-1100 nm indicated that light is smaller absorbed inside CIGS bulk, actually it was deteriorated when using higher aqua regia concentrations. The morphology and structure of CIGS films was clearly changed via observing their SEM images. Hence, the varied aqua regia concentrations become the other key parameters.

CHAPTER V

SUMMARY

This thesis presents the wet-chemical etching (WCE) process on CIGS thin film surfaces for solar cell application. The samples of CIGS thin film were grown by three-stage co-evaporation technique with fixed $x = [\text{Ga}]/([\text{Ga}]+[\text{In}])$ and $y = [\text{Cu}]/([\text{Ga}]+[\text{In}])$. The methods to etch the CIGS surfaces have been studied by using commonly used chemical solutions such as aqua regia, potassium hydroxide (KOH), and alcoholic potassium hydroxide (KOH+EtOH). The roughness of CIGS surface has an important role affecting solar cell properties such as p-n junction formation and especially solar cell parameters.

There are three main parts of the results in order to study the relationship between the roughness of CIGS surfaces and the solar cell parameters and also spectral responses.

- Surface morphology and rms roughness:

Using aqua regia etching could effectively alter the surface of CIGS films. Conversely, potassium hydroxide and also alcoholic potassium hydroxide tend to have no significant effects. The various CIGS surface roughness can be suitably obtained from aqua regia etching condition with varying concentrations and etching times. The different rms roughness values were studied. Noticeably, any pored CIGS surfaces probably act as a defect that occurs after the deposition of CdS layer, leading to lower device performance. The number of pores increase at longer etching duration. The occurrence of pores usually happens around grain boundaries. Etching more than a minute decreases the thickness of CIGS film and has high probability to leave more chemical residues. In order to reveal more detail about surface compositions of etched CIGS surfaces, it needs to use the other characterization techniques such as secondary ion

mass spectrometer (SIMS) or equivalent tools which may be a future work.

- J–V curves:

Potassium hydroxide and alcoholic potassium hydroxide etching conditions show worse J-V curves than the non-etched condition. The surface roughness features clearly impact solar cell parameters, especially J_{sc} and efficiencies. By using 1:1 concentration ratio of aqua regia : deionized water at 4 s with 71 nm of rms roughness value (AR24_13), it tends to result in an increase of efficiency at about 13.4%. Although, it did not achieve very high efficiency. But J_{sc} , V_{oc} , and R_{sh} are significantly increased. Increasing of R_{sh} means the quality of p-n junction could be enhanced. Smoother CIGS surfaces and also very rough CIGS surface tend to produce lower efficiencies, J_{sc} , and fill factor, but higher V_{oc} .

- Spectral responses:

The EQE curves of potassium hydroxide and alcoholic potassium hydroxide etching conditions are not better than the non-etched condition. Especially, potassium hydroxide etching conditions never help to alter the CIGS surface, actually worsen the situation. Even the surface roughness did not change, perhaps it affects chemical compositions at CIGS surfaces, leading to lower EQE curves. Briefly, the main optical loss mechanisms come from the recombination at CdS/CIGS interface and incomplete carrier collection in CIGS bulk. The aqua regia conditions at a few seconds of etching times of 1:1 ratio result in an improvement at short wavelength about 550 nm. It means that the CdS/CIGS interface is enhanced which can reduce the interface recombination, thus generate more photocurrent. The altered CIGS surfaces with pores result in lower EQE curves.

REFERENCES

1. Chu, Y., *Review and comparison of different solar energy technologies*. August 2011, Research associate, Global Energy Network Institute (GENI).
2. *Photovoltaics*. [World Wide Web] 8 May 2016]; Available from: <https://en.wikipedia.org/wiki/Photovoltaics>.
3. Perlin, J., *Space to Earth: The Story of Solar Electricity*. 2002: Harvard University Press.
4. Liao, D. and A. Rockett, *Cd doping at the CuInSe₂/CdS heterojunction*. *Journal of Applied Physics*, 2003. **93**(11).
5. Scheer, R., et al., *Cu(In_{1-x}G_x)Se₂ growth studies by in situ spectroscopic light scattering*. *Applied Physics Letters*, 2003. **82**(2091).
6. Y., L.T., et al., *Characterisations of CdS thin films deposited on glass and Cu(In,Ga)Se₂ layer using chemical bath deposition*. *Thin Solid Films*, 2013. **548**: p. 64-68.
7. Wakeling, B.R., et al., *In situ analysis of cadmium sulphide chemical bath deposition by an optical fibre monitor* *Thin Solid Films*, 2012. **525**: p. 1-5.
8. M., P.S., et al., *Junction formation at the interface of CdS/CuIn_xGa_(1-x)Se₂*. *Journal of Physics D: Applied Physics*, 2014. **47**(345302 (8pp)).
9. Shafarman, W.N. and L. Stolt, *Cu(InGa)Se₂ Solar Cells*, in *Handbook of Photovoltaic Science and Engineering*, A. Laque and S. Hegedus, Editors. 2003, John Wiley & Sons, Ltd. p. 567-616.
10. Shafarman, W.N., R.S. Huang, and S.H. Stephens, *Characterisation of Cu(InGa)Se₂ solar cells using etched absorber layers*, in *The 2006 IEEE 4th World Conference on Photovoltaic Energy Conversion*. 2006: Oakland, California, USA. p. 420-423.
11. Abou-Ras, D., et al., *Structural and chemical investigations of CBD- and PVD-CdS buffer layers and interfaces in Cu(In,Ga)Se₂-based thin film solar cells*. *Thin Solid Films*, 2005(480-481): p. 118-123.
12. Merdes, S., et al., *Zn(O,S) buffer prepared by atomic layer deposition for sequentially grown Cu(In,Ga)(Se,S)₂ solar cells and modules*. *Solar Energy Materials & Solar Cells*, 2014. **126**: p. 120-124.
13. Altosaar, M., et al., *Further developments in CIS monograin layer solar cell technology*. *Solar Energy Materials & Solar Cells*, 2005. **87**: p. 25-32.
14. Canava, B., et al., *Chemical elaboration of well defined Cu(In,Ga)Se₂ surfaces after aqueous oxidation etching*. *Journal of Physics and Chemistry of Solids* 2003. **64**: p. 1791-1796.
15. Perrin, W. and W.H. Tarn, *Handbook of metal etchants*. 1991: CRC Press. 1415.
16. McCandless, R.W.B.a.B.E., *Specular CuInSe₂ films for solar cells*. *Appl. Phys. Lett.*, 1988. **53**(2): p. 140-141.
17. Delsol, T., M.C. Simmonds, and I.M. Dharmadasa, *Chemical etching of Cu(In,Ga)Se₂ layers for fabrication of electronic devices*. *Solar Energy Materials & Solar Cells*, 2003. **77**: p. 331-339.
18. Kauk, M., et al., *Chemical etching of CuInSe₂ absorber surface for monograin layer solar cell application*. *Solar Energy Materials & Solar Cells*, 2005. **87**: p. 25-32.

19. Jehl, Z., et al., *Thinning of CIGS solar cells: Part II: Cell characterizations*. Thin Solid Films, 2011. **519**: p. 7212-7215.
20. Jehl, Z., et al., *In sight on the influence of surface roughness on photovoltaic properties of state of the art copper indium gallium diselenide thin film solar cells*. Journal of Applied Physics, 2012. **111**(114509).
21. Y-C, W., et al., *Large-scale micro- and nanopatterns of Cu(In,Ga)Se₂ thin film solar cells by mold-assisted chemical-etching process*. ACS nano, 2015. **9**(4): p. 3907-3916.
22. Rattley, M., *Ambiguous bromine*. Nature Chemistry, 2012. **4**(512).
23. Slobodskyy, A., et al., *In-depth analysis of CIGS film for solar cells, structural and optical characterization*. Applied Physics Letters, 2010. **97**(251911).
24. Neamen, D.A., *Semiconductor physics and devices*. 4th ed. 2012: McGraw-Hill
25. Sukaïem, S., *Quantum efficiency measurements of CuIn_{1-x}Ga_xSe₂ solar cells*, in *Department of Physics, Faculty of Science*. 2014, Chulalongkorn University. p. 63.
26. Gifford, J. *Solar Frontier hits 22.3% on CIGS cell*. [World Wide Web] 2015 18 Mar 2016]; Available from: http://www.pv-magazine.com/news/details/beitrag/solar-frontier-hits-223-on-cigs-cell_100022342/#axzz4ADl6rVuy.
27. Jackson, P., et al., *Effects of heavy alkali elements in Cu(In,Ga)Se₂ solar cells with efficiencies up to 22.6%*. Physica Status Solidi RRL, 2016. **1-4**.
28. Dharmadasa, I.M., *Fermi level pinning and effects on Cu(In,Ga)Se₂-based thin film solar cells*. Semiconductor Science and Technology, 2009. **24**(055016).
29. Jackson, P., et al., *Properties of Cu(In,Ga)Se₂ solar cells with new record efficiencies up to 21.7%*. Physica Status Solidi RRL, 2015. **9**: p. 28-31.
30. Kessler, J., et al., *Cu(In,Ga)Se₂ Thin Films Grown with a Cu-Poor/Rich/Poor Sequence: Growth Model and Structural Considerations*. Progress in Photovoltaics: Research and Applications, 2003. **11**: p. 319-331.
31. Kessler, J., et al., *Growth of Cu(In,Ga)Se₂ film using a Cu-poor/rich/poor sequence: substrate temperature effects*. Thin Solid Films, 2003(431-431): p. 1-5.
32. Gabor, A.M., et al., *High efficiency CuIn_xGa_{1-x}Se₂ solar cells made from (In_xGa_{1-x})₂Se₃ precursor films*. Applied Physics Letters, 1994. **65**(2): p. 198-200.
33. Butsriruk, K., *Fabrication of CIGS thin film solar cells by selenization of metallic layers*, in *Department of Physics, Faculty of Science*. 2014, Chulalongkorn University. p. 46.
34. *Aqua regia*. [World Wide Web] 10 May 2016]; Available from: https://en.wikipedia.org/wiki/Aqua_regia.
35. *Potassium hydroxide*. [World Wide Web] 10 May 2016]; Available from: https://en.wikipedia.org/wiki/Potassium_hydroxide.
36. Wefringhaus, E. and A. Helfricht. *KOH/surfactant as an alternative to KOH/IPA for texturisation of monocrystalline silicon*. in *24th European Photovoltaic Solar Energy Conference*. 2009. Hamburg, Germany.

37. Ho W-J, S.S.-Y., Lee Y-Y, Syu H-J, Lin C-F, *Performance-enhanced textured silicon solar cells based on plasmonic light scattering using silver and indium nanoparticles*. *Materials*, 2015. **8**(10): p. 6668-6676.
38. Goldstein, J.I., et al., *Scanning electron microscopy and x-ray microanalysis*. Third ed. 2003: Springer.
39. Hughes, D.L. *What is an electron microscope?* [World Wide Web] 20 May 2016]; Available from: <http://www.biologicalelectronmicroscopy.com/introduction-to-biological-electron-microscopy.html>.
40. Bernardini, C., et al., *Colloids in Flatland: a perspective on 2D phase-separated systems, characterisation methods, and lineactant design*. *Chemical Society Review*, 2013. **42**: p. 2100-2129.



APPENDIX



VITA

Tanchanok Muifeang was born on 29th March 1991 in Bangkok, Thailand. He received the Bachelor degree of Science in Applied Physics (Nano-material technology) from department of Physics, faculty of Science, King Mongkut's University of Technology Thonburi in 2013.

